Contreras Hidalgo, C., Cashman, K. V., Rust, A. C., & Cortex, M. (2022). The influence of magma storage and ascent conditions on Laguna del Maule rhyolite eruptions. *Journal of Petrology*, *63*(12), [egac121]. https://doi.org/10.1093/petrology/egac121

University of Bristol - Explore Bristol Research
General rights

The Influence of Magma Storage and Ascent Conditions on Laguna del Maule Rhyolite Eruptions

Claudio Contreras [iD][1],*, Katharine V. Cashman[1], Alison Rust[1] and Marcelo Cortés[2,3]

[1]School of Earth Sciences, University of Bristol, Wills Memorial Building, Queen's Road, Bristol BS8 1RJ, UK.
[2]Departamento de Geología, Facultad de Ciencias Físicas y Matemáticas, Universidad de Chile, 803 Plaza Ercilla, 8370450 Santiago, Chile.
[3]Centro de Excelencia en Geotermia de los Andes (CEGA), Facultad de Ciencias Físicas y Matemáticas, Universidad de Chile, 803 Plaza Ercilla, 8370450 Santiago, Chile.

*Corresponding author at: claudio.contrerashidalgo@bristol.ac.uk, +44 7956 085318

Abstract

The scarcity of historical rhyolite eruptions means that volcanological and petrological studies of past eruptions are a key tool for assessing the potential for future hazardous activity and improving interpretations of unrest signals. For the last 18 ky, the Laguna del Maule (LdM) volcanic complex in Chile has erupted primarily rhyolites but with differing magma compositions, eruption styles and eruptive volumes. Rapid surface uplift and episodic seismic activity at LdM over the last two decades has emphasized the need to understand both the recent evolution of the magmatic system and the most likely future eruption scenarios. Using mineral composition, geothermobarometry and MELTS modeling, we assess the influence of the magma storage and ascent conditions on the magnitude and styles of three LdM rhyolites. Magmas of the first and largest Plinian-ignimbrite eruption (LdM: *rdm*; >17 km^3 DRE) form a distinct mineral assemblage with An$_{28-60}$ plagioclase, amphibole and quartz derived from a magma plumbing system over a large pressure range (90–350 MPa). We suggest that the *rdm* eruption was triggered by magma recharge and overpressure within a ~90 MPa magma chamber of high-silica (>76.5 wt.% SiO$_2$) rhyolitic melt. The *rdm* eruption appears to have reset the LdM storage conditions, such that subsequent rhyolite eruptions have been smaller (<4 km^3 DRE), involved less evolved melt (<75.8 wt.% SiO$_2$) and produced (sub)Plinian-effusive eruption sequences. Of these, we have studied the earliest (Los Espejos: *rle*) and the most recent (Las Nieblas: *rln*). Both have mineral assemblages with An$_{20-34}$ plagioclase and biotite formed in water-saturated crystal-poor rhyolite batches over limited pressure ranges (ΔP ~50 MPa) within a rhyodacitic mush reservoir. We suggest that *rle* and *rln* were triggered by injection of water-rich magma and volatile exsolution; the transition to effusive behavior occurred because of changes in magma temperature (*rle*) or magma decompression rate (*rln*). Similarities in the limited pressure range and high volatile content inferred for the current low-density magma body with the petrologically determined source conditions of magmas that fed past subplinian-effusive eruptions suggest that the next LdM eruption will be similar.

Keywords: High-silica magmas, Laguna del Maule volcanic complex, magma storage conditions, plagioclase composition, silicic eruptive transitions

INTRODUCTION

Silicic magmatic systems have the potential to produce a wide range of eruption styles, from devastating caldera-forming explosive eruptions to relatively benign obsidian lava flows (Self, 2006; Self & Blake, 2008). Challenges in monitoring these systems stem from the scarcity of historical rhyolitic eruptions, the need to distinguish between hydrothermal and magmatic signals, the limited precursors before some silicic eruptions, and the potential for rapid changes in eruptive style during a single eruptive episode (Castro & Dingwell, 2009; Schipper *et al.*, 2013; Biggs & Pritchard, 2017). Understanding controls on eruptive style, including behavioral transitions, is a key challenge. During a single eruption, transitions are controlled primarily by changes in shallow processes, such as vesiculation, crystallization and outgassing; changes in the style over several eruptions may reflect changing conditions of magma storage and initial ascent (Cassidy *et al.*, 2018).

Tephra and lava samples can provide clues to the factors controlling the diversity of eruption styles in silicic volcanic fields (e.g. Wotzlaw *et al.*, 2014; Barker *et al.*, 2016; Wilson, 2017; Andersen *et al.*, 2018). Petrologic data indicate that many silicic magma systems reside in the shallow crust as crystal-rich (>50% crystals) mush reservoirs that are incubated over thousands to tens of thousands of years but are too viscous to erupt in bulk (Bachmann & Bergantz, 2004; Jackson *et al.*, 2018; Andersen *et al.*, 2019; Hildreth, 2021). Eruptible crystal-poor rhyolite melt bodies can form within these mush bodies because of internal (melt extraction by compaction and/or volatile-driven segregation) or external (recharge by deeper magma) processes (Bachmann & Bergantz, 2004; Bindeman & Simakin, 2014; Cashman *et al.*, 2017; Brahm *et al.*, 2018) that may act over time scales of months to centuries (Wark *et al.*, 2007; Druitt *et al.*, 2012; Till *et al.*, 2015; Andersen *et al.*, 2018). Evidence for eruption triggers can be found in resulting deposits as mafic to intermediate enclaves (magma recharge), heterogeneities in whole-rock trace elements due to amalgamation of discrete rhyolite bodies, crystallinity (crystal fractionation), mineral composition (storage and ascent conditions) and crystal textures (Gelman *et al.*, 2013; Till *et al.*, 2015; Barboni *et al.*, 2016; Andersen *et al.*, 2017, 2019; Rubin *et al.*, 2017).

The Laguna del Maule (LdM) volcanic complex is a caldera-forming system straddling the Chile-Argentina border in the
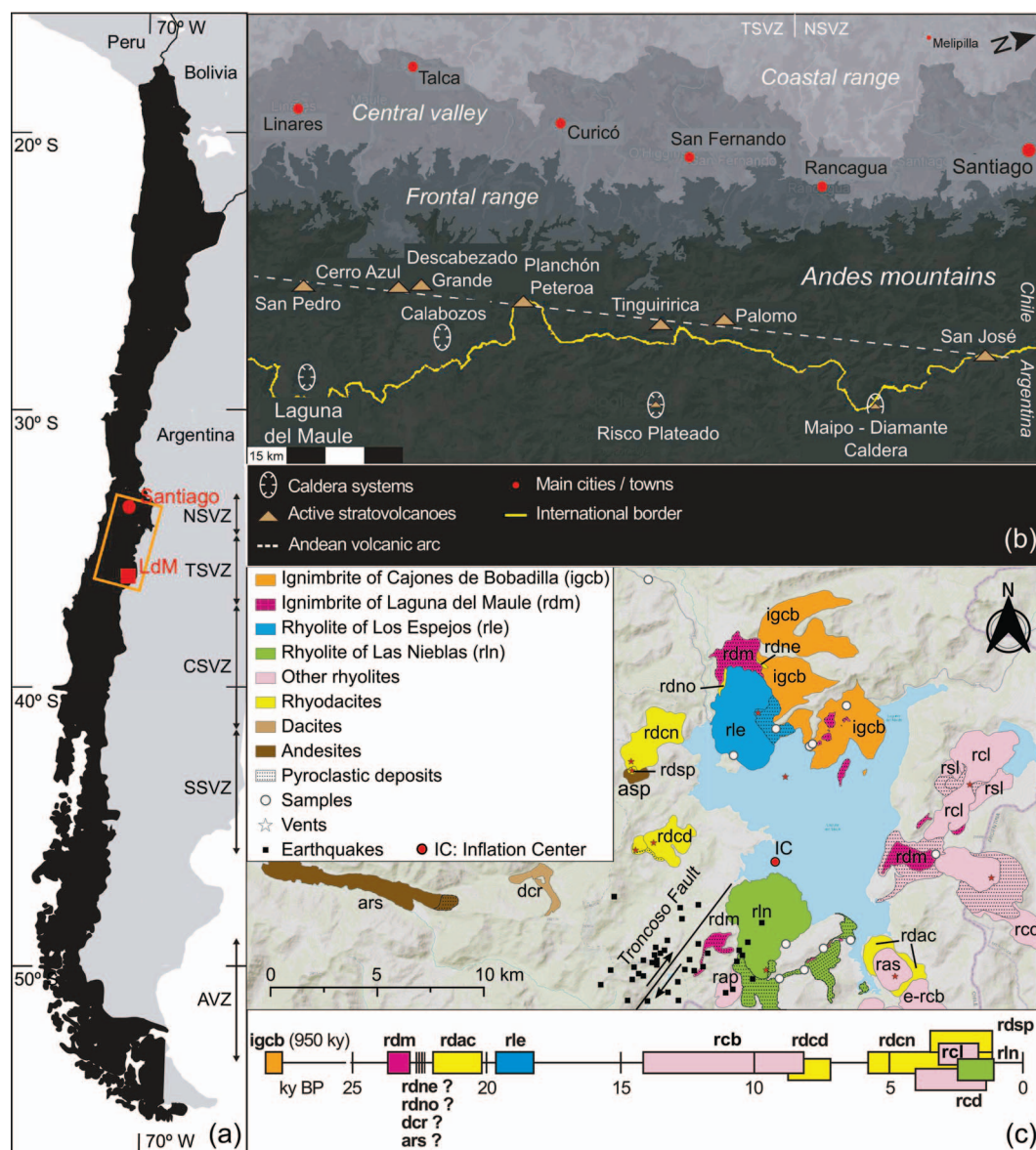
Fig. 1. Geological context of the LdM volcanic complex. (a) Map of Chile showing the Andean Southern and Austral volcanic zones (SVZ and AVZ, respectively) according to López-Escobar *et al.* (1995). For the SVZ, N- = North; T- = Transitional; C- = Central; S- = South. The orange rectangle marks (b). (b) View of Central-South Chile showing the main geomorphological units. The volcanic arc consists of stratovolcanoes of intermediate compositions. The caldera systems are 10–30 km east of the arc under a back-arc extensional regime. (c) The LdM volcanic complex showing the three rhyolites studied and other eruptions mentioned in this paper. Ages by $^{40}Ar/^{39}Ar$ are from Hildreth *et al.* (2010) and Andersen *et al.* (2017).

locally extending rear-arc of the Transitional Southern Volcanic Zone of the Andes (Fig. 1a,b; López-Escobar *et al.*, 1995; Cembrano & Lara, 2009). In the last two decades, rapid surface inflation (∼20–30 cm per year) 5 km north of the most recent eruptive vent (Feigl *et al.*, 2014; Le Mével *et al.*, 2021) and episodic seismic activity ∼10 km SW of the inflation center (Garibaldi *et al.*, 2020; Sernageomin, REAV, 2020, 2021; Fig. 1c) have made LdM a target for investigating the generation and eruption of rhyolite magma. However, it still remains uncertain whether the unrest signals are precursors to an eruption, and if so, the most likely magnitude and eruption style(s). Here we address this question by studying the preeruptive storage conditions of three key eruptive units: the caldera-forming LdM eruption (*rdm*; 17 ka), the first post-*rdm* subplinian-effusive eruption (Los Espejos, *rle*; 12 ka) and the most recent subplinian-effusive eruption (Las Nieblas, *rln*; 1.8 ka; Fierstein, 2018).

BACKGROUND
Postglacial eruption record of the LdM volcanic complex

Since the Patagonia deglaciation (∼18 ky), LdM has produced >40 rhyolites from at least 24 separate vents (Hildreth *et al.*, 2010; Fierstein, 2018; Hildreth, 2021). The first is the plinian-ignimbrite rhyolite of LdM (*rdm*). The explosive (pyroclastic fall and flow) deposits from this eruption extend ≤100 km east into Argentina; proximal to medial deposits typically comprise low-density and almost aphyric pumice clasts. The *rdm* deposit is also the only postglacial rhyolite to include mafic juveniles, mafic enclaves and granitoid lithics, all of which increase upward in the *rdm* eruption sequence (Contreras-Hidalgo, 2020). The smaller (<4 km³ DRE) post-*rdm* rhyolites include both explosive (fall and flow) and effusive activity (Hildreth *et al.*, 2010; Gho *et al.*, 2019). Both the small volumes of the tephra deposits and the textural variations
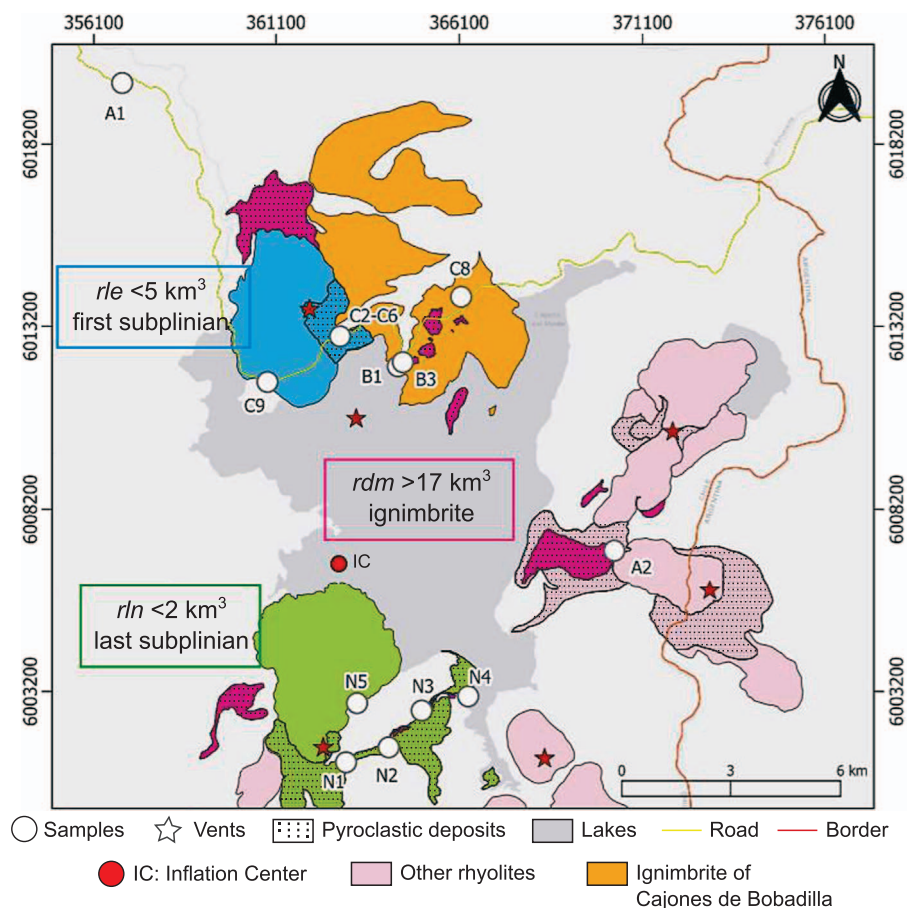
Fig. 2. Map of *rdm*, *rle* and *rln* and sample location. The proximal deposits of the rhyolites studied, and their vents are highlighted together with other postglacial rhyolites, the ignimbrite of Cajones de Bobadilla (*igcb*), the international road and border for geographical reference. Colors are the same as Fig. 1.

in the post-*rdm* pumice suggest subplinian to moderate Plinian activity (Gho *et al.*, 2019; Contreras-Hidalgo, 2020). Effusive activity produced rhyolitic lava flows with volumes of 0.4 to 1.16 km³ DRE (Cáceres *et al.*, 2018). The *rle* eruption sequence consists of a < 3 km³ (bulk) pyroclastic fall deposit and a bilobate lava flow (0.82 km³); the fall deposit contains pyroclastic obsidian that increases in abundance toward the top of fall deposit (Contreras-Hidalgo, 2020). The *rln* eruption sequence is more complex with a pyroclastic fall deposit (<1 km³ bulk), a pyroclastic flow (~0.17 km³ DRE), two lava flows (1.16 km³) and two minor ejecta cones.

Petrology of the LdM volcanic complex

LdM has erupted predominantly rhyolite in the last 18 ky (postglacial era), with ~34 km³ rhyolitic tephra and lavas (26.5 km³ DRE and 7.8 km³, respectively; Fierstein, 2018; Hildreth, 2021) compared to 2.1 km³ of intermediate composition (rhyodacitic to andesitic) magma. *Rdm* is the only postglacial high-silica (>76 wt.% SiO_2) rhyolite and is one of two rhyolites having both hornblende as the main mafic hydrous phase and mafic enclaves (the other is a low silica rhyolite with petrographic features of rhyodacites; Hildreth *et al.*, 2010). All the post-*rdm* rhyolites, in contrast, have <75.8 wt% SiO_2 and contain phenocrysts of plagioclase and biotite.

Although having the same mineralogy, the LdM post-*rdm* rhyolites show subtle time-dependent variations of whole-rock compositions, plagioclase compositions and magma temperature

(Andersen *et al.*, 2018; Hildreth, 2021). The first post-*rdm* rhyolite, *rle,* is the most silicic (75.7 wt.% SiO_2; Hildreth *et al.*, 2010), contains oligoclase (An$_{21-23}$; Andersen *et al.*, 2018) and an average two-oxide temperature of 763°C (Andersen *et al.*, 2017). The most recent rhyolite *rln*, in contrast, has 73.4 wt.% SiO_2 (Hildreth *et al.*, 2010), more anorthitic plagioclase (An$_{20-34}$; Andersen *et al.*, 2018) and is hotter (average of 793°C by two-oxide thermometry; Andersen *et al.*, 2017). Estimated storage pressures for *rle* and *rln* samples are limited to some tens of MPa (170–220 and 160–220 MPa, respectively; Klug *et al.*, 2020). These data suggest that persistent magma recharge has increased the temperature of the mush reservoir over time and incubated localized regions with rhyolitic melt (Andersen *et al.*, 2019).

Time constraints, including zircon geochronology (Andersen *et al.*, 2019) and Sr-Mg diffusion chronometry in plagioclase (Andersen *et al.*, 2018), indicate that an upper-crustal (<2.5 kbar) crystal-rich reservoir has been active for the last 34 to 160 ky but that individual batches of rhyolite magma accumulate only decades to centuries before eruption. Limited pressure ($\Delta P < 70$ MPa) and temperature ($\Delta T < 60°C$) ranges estimated by thermobarometry (Andersen *et al.*, 2017, 2018; Cáceres *et al.*, 2018) suggest that small individual rhyolite batches are stored within the crystal mush. The common long-lived source region for rhyolite magma and the limited P–T ranges of melt storage explain the similarity of whole-rock major element compositions and the observed plagioclase-biotite assemblage in most post-*rdm* rhyolites (Hildreth *et al.*, 2010; Andersen *et al.*, 2017). This

Table 1: Averages of groundmass glass compositions measured by EMPA[1] of pumices, pyroclastic obsidians and lavas from *rdm*, *rle* and *rln*

Sample Type	SiO_2	TiO_2	Al_2O_3	FeO	MnO	MgO	CaO	Na_2O	K_2O	P_2O_5	SO_2	Cl
Rhyolite of LdM (rdm)												
WR	76.7	0.15	12.93	0.72	0.05	0.1	0.58	3.71	4.62	0.07	n.d.	n.d.
PF P	77.22	0.11	12.9	0.57	0.04	0.1	0.54	4.16	4.2	0.02	0.01	0.13
FD P	76.91	0.13	13.08	0.7	0.04	0.11	0.64	3.8	4.39	0.03	0.02	0.13
Rhyolite of Los Espejos (rle)												
WR	75.7	0.18	13.23	0.87	0.07	0.12	0.64	4.27	4.44	0.05	n.d.	n.d.
Pum.[2]	76.3	0.15	13.27	0.74	0.06	0.09	0.59	4.31	4.33	0.02	0	0.15
Obs.[3]	76.38	0.15	13.21	0.77	0.06	0.1	0.59	4.28	4.33	0.01	0	0.14
Lava	76.42	0.15	13.14	0.76	0.07	0.1	0.59	4.4	4.33	0.02	0	0.13
Rhyolite of Las Nieblas (rln)												
WR	73.4	0.26	14.6	1.19	0.08	0.22	0.8	4.89	4.09	0.05	n.d.	n.d.
Pum.[4]	75.25	0.19	13.9	0.93	0.07	0.16	0.61	4.31	4.2	0.03	0	0.16

Whole-rock (WR) major element compositions also provided for reference. PF P = Pyroclastic flow pumice; FD P = Fall deposit pumice; Pum. = Pumice; Obs. = Pyroclastic obsidian.
[1]The averages correspond to 37–55 points per pyroclast / rock.
[2]Averages from 3 pumice clasts.
[3]Averages from 2 obsidian clasts.
[4]Averages from 4 pumice clasts.

hypothesis, however, does not explain the mafic juveniles, granitoid lithics, and different mineral assemblage (An_{41-59} plagioclase, hornblende and quartz) observed in the *rdm* Plinian-ignimbrite rhyolite.

Geophysical imaging of the LdM magmatic system

Geophysical imaging provides insights into properties of the subsurface. Geophysical imaging at LdM has included gravity (Miller *et al.*, 2017; Trevino *et al.*, 2021), magnetotellurics (Cordell *et al.*, 2018, 2020) and surface-wave and teleseismic tomography (Wespestad *et al.*, 2019; Bai *et al.*, 2020). Together these data show that LdM overlies a magmatic and hydrothermal plumbing system of 0–14 km depth (0–350 MPa) and 350 km^2 aerial extent within a crystal-rich (85–95% crystals) silicic mush framework (Cordell *et al.*, 2020).

The magma reservoirs forming the LdM plumbing system are interpreted using three crystallinity ranges, independent of the magma or mush composition, as melt-rich (<15% crystals) and potentially eruptible magma batches; mush with extractable melt (50–75% crystals) and a rigid sponge (>85% crystals; Andersen *et al.*, 2018; Cordell *et al.*, 2020). Surface-wave tomography shows a low-shear-wave velocity anomaly at 2–8 km-depth (50–200 MPa) interpreted as a 450 km^3 rigid sponge with ~5% poorly connected interstitial melt (Wespestad *et al.*, 2019). Similarly, p-wave tomography suggests a low velocity anomaly at 0 to 12 km-depth (0–300 MPa) that is consistent with a 500 km^3 rigid sponge with 14% interstitial melt (Bai *et al.*, 2020). Magnetotelluric and gravity surveys show low-resistivity and low-density regions interpreted as discrete silicic batches and lenses within the larger crystal-rich reservoir (Miller *et al.*, 2017; Cordell *et al.*, 2018, 2020; Trevino *et al.*, 2021), although anomalous regions found by magnetotellurics and gravity do not overlap. Below the Los Espejos lava flow at 4 to 7.5 km (100–190 MPa), a low resistivity region imaged by magnetotellurics is interpreted as a hydrous (~5 wt.% H_2O) mush reservoir with rhyolitic melt (65% crystals; Cordell *et al.*, 2020). 2.5 km south and below the inflation center at 70 to 120 MPa (2.8–4.8 km-depth), a 30-km^3 low density region imaged by gravity is interpreted as a volatile-rich, melt-rich rhyolite (Miller *et al.*, 2017). Two overlying shallow (<1 km), high-conductivity regions

are interpreted as high-salinity hydrothermal reservoirs or clay-bearing sediments with high cation exchange capacity (Cordell *et al.*, 2018).

A variety of sources have been considered for the current inflation including the shallow (<1 km), high-conductivity regions, the 70- to 120-MPa low density region or a sill just below the crystal mush reservoir (Feigl *et al.*, 2014; Miller *et al.*, 2017; Rojas *et al.*, 2022). This raises the question of whether the current unrest will lead to an eruption and if yes, the source and style of the resulting activity.

Here we add to the existing studies by comparing the magma storage conditions (P, T, H_2O) of *rdm*, *rle* and *rln* inferred from petrologic analysis and MELTS modeling with the plumbing system imaged by geophysics to assess the potential hazards related to the current volcanic unrest. Constraints on magma storage are provided by mineral compositions, textures of phenocrysts and microcrysts, hornblende thermobarometry, plagioclase hygrometry and MELTS simulations. We sampled different levels of the eruption sequences and analyzed both pumice clasts and lava samples to determine the role of the storage and ascent conditions in the styles of, and transitions between, different eruption phases. To gain insights into the deeper parts of the magmatic system, we sampled *rdm* pumice clasts from the top of the pyroclastic fall deposit and from proximal regions of the pyroclastic flow deposits (Fig. 2) that contain a higher fraction of mafic juveniles and enclaves.

METHODOLOGY
Sampling and analytical methods

Fifteen samples were analyzed petrographically: three pumice clasts of late-erupted *rdm*, three pumice clasts and three obsidian clasts from the *rle* fall deposit, two samples of *rle* lava, three pumice clasts from the *rln* pyroclastic flow, and one sample of *rln* lava. Sample locations are summarized in Figure 2. One *rdm* pumice clast was selected from each of (1) a pyroclastic flow outcrop on the side of the international Talca-Paso Pehuenche road located 5 km northwest of Los Espejos vent (A1 in Fig. 2), (2) a pyroclastic flow at a beach on the north shore of the lake (B1 in Fig. 2), and (3) the top of a fall deposit sequence west of the Divisoria lava flow (A2 in Fig. 2). The three *rdm* pumice clasts vary
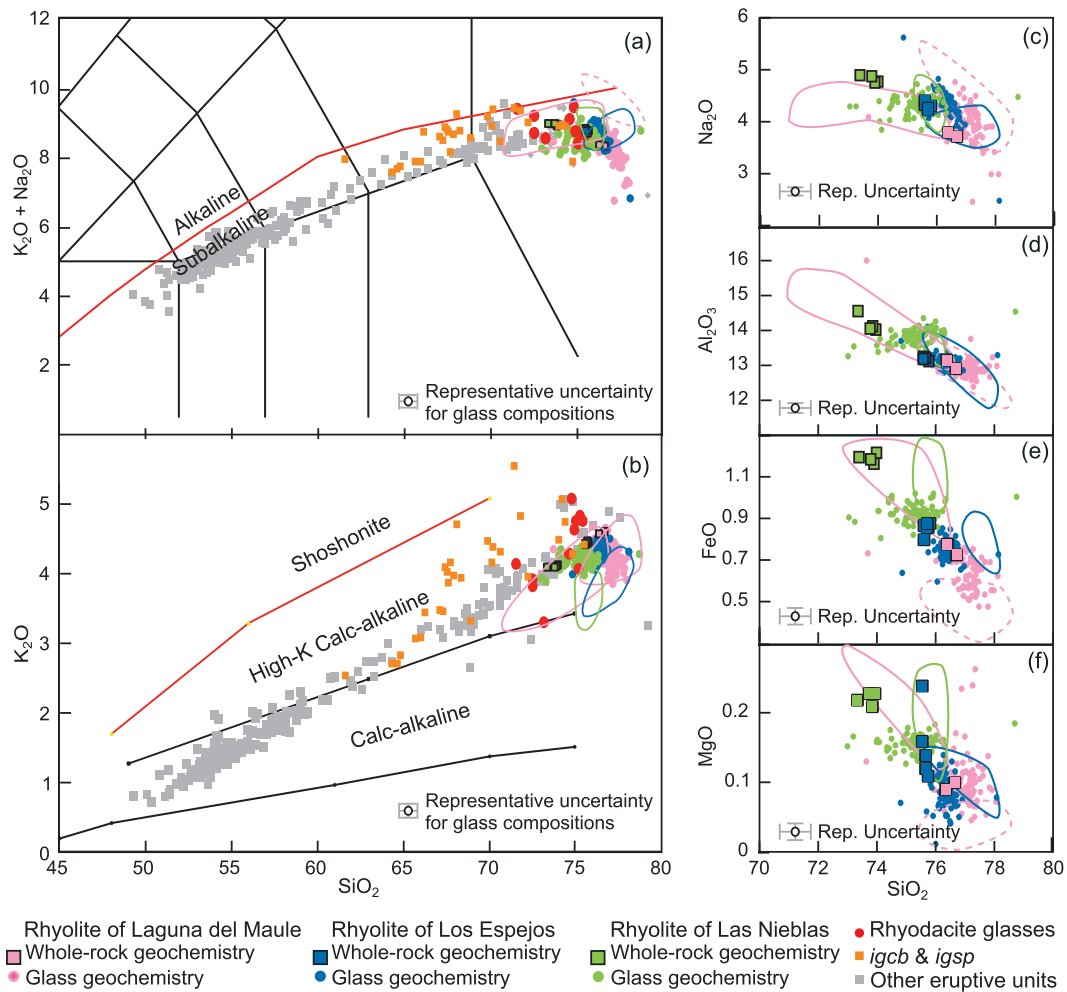
Fig. 3. Whole rock and glass geochemistry of the LdM volcanic complex. (a) Total alkali versus silica classification diagram after Le Bas *et al.* (1986). (b) K₂O vs SiO₂ diagram after Peccerillo & Taylor (1976). (c)-(f) Harker diagrams of Na₂O, Al₂O₃, FeO and MgO with SiO₂. Whole rock geochemistry data from Hildreth *et al.* (2010) and Andersen *et al.* (2017); glass geochemistry data are new except the rhyodacite data from Cáceres *et al.* (2018); outlines mark the extent of plagioclase-hosted (solid line) and quartz-hosted (dashed line) melt inclusion anhydrous geochemistry data for the same eruptions (indicated by colour) from Klug *et al.* (2020). The largest tertiary ignimbrites corresponding to the ignimbrite of Cajones de Bobadilla (*igcb*) and the ignimbrite of Sin Puerto (*igsp*) are highlighted.

in density and fabric (isotropic to tube pumice). Two pairs of *rle* fall pumice and obsidian clasts come from a perlite mine located 1 to 2 km from the vent (C2–6 in Fig. 2), one pair from the upper obsidian-rich sequence and the other from the middle pumice-rich sequence; a third *rle* clast pair comes from the top of the fall deposit in a valley located 3 km east of the vent (B3 in Fig. 2). The three *rln* pumice clasts come from a pyroclastic flow sampled at different distances from the vent (N1–3 in Fig. 2); a lava sample was collected from the eastern border of the younger lava flow (N5 in Fig. 2).

Backscatter electron (BSE) images were collected by scanning electron microscopy (Hitachi S3500) at the University of Bristol using an accelerating potential of ~15 kV and electron beam current of 50 to 60 nA. Major and minor element compositions of plagioclase, K-feldspar, amphibole, biotite and groundmass glasses were performed from polished thin sections and polished pumice mounts on a Cameca SX100 electron microprobe equipped with five wavelength-dispersive spectrometers at University of Bristol using an accelerating potential of 20 keV, an electron beam current of 10 nA for crystals and 6 nA for groundmass glass, and a beam defocused to 2 μm. Natural and synthetic mineral standards were used for primary calibration, and mineral and

anhydrous glasses were used as secondary standards to check the accuracy of the calibration. All compositions, standard deviations and detection limits of plagioclase, K-feldspar, biotite, amphibole and groundmass glass and the calibration and standard material used to assess data quality are provided in the Supplementary Material.

The data set of plagioclase and K-feldspar was collected using on-peak count times of 10 s for Si, Al, Na, K and Ca, and 60 s for Mg, Fe, Sr and Ba. Estimated uncertainties in the measurements were < 1% for Si, ~1% for Al, ~2% for Ca, ~3% for Na, ~6% for K, ~13% for Fe, 33–55% for Ba, 55–95% for Sr and > 100% for Mg. Analyses with totals <98.5 and > 101.5% were discarded.

The following on-peak count times were used on biotite, amphibole, and groundmass glass: 10 s for Si, K and Ti, 20 s for Al, 30 s for Na, Ca, Mg, Fe and Mn, and 60 s for Ba. Estimated uncertainties in both mafic minerals and groundmass glass were ~ 1% for Si and Al, and 2% for K; in the other elements, the uncertainties vary for mafic minerals and groundmass glasses, respectively: 5% and 2% for Na, 1% and 5% for Fe, 1% and 12% for Mg, 3% and 20% for Ti, >100% and 3% for Ca, 8% and 35% for Mn, and 12% and 50% for Ba. Totals of <97% (<95% for mafic hydrous minerals) and > 101.5% were discarded. Background count times

Table 2: Crystal size, shape, and occurrence of clusters and microcrysts for *rdm*, *rle* and *rln*

Phase	Maximum size [mm]	Shape	Clots	Microcrysts
Rhyolite of LdM (rdm)				
Plagioclase	0.3	Anhedral to subhedral	Plagioclase and hornblende	No
Hornblende	0.3	Euhedral	Plagioclase and hornblende	No
Ti-Magnetite	0.1	Subhedral	Oxides	–
Ilmenite	0.1	Subhedral	Oxides	–
Olivine	0.2	Anhedral	In mafic blobs	No
Clinopyroxene	0.2	Anhedral	In mafic blobs	No
Apatite	0.1	Euhedral	Plagioclase	–
Zircon	0.1	Subhedral	No	–
Rhyolite of Los Espejos (rle)				
Plagioclase	1.8	Subhedral to euhedral	All the other phases	In pumices and obsidians
Biotite	0.8	Anhedral (pumices) or Euhedral (obsidians)	Plagioclase	In obsidians
Ti-Magnetite	0.1	Subhedral	Oxides	–
Ilmenite	0.1	Subhedral	Oxides	–
Apatite	0.1	Euhedral	Plagioclase	–
Zircon	0.1	Subhedral	No	–
K-feldspar	0.2	Skeletal	Plagioclase	In pumices
Rhyolite of Las Nieblas (rln)				
Plagioclase	3	Subhedral	Plagioclase	In obsidians
Biotite	3.5	Euhedral	No	In obsidians
Ti-Magnetite	0.3	Subhedral	Plagioclase, biotite, oxides	–
Ilmenite	0.1	Anhedral	Oxides	–
Apatite	0.1	Euhedral	Plagioclase	–
Zircon	0.1	Subhedral	No	–

at each side of the peak were half on-peak count times for each element analyzed for all materials analyzed.

Spot analyses of both hornblende cores and rims were used for thermobarometry. Spot analyses and compositional traverses with 15–30 μm-spacing were collected for major and minor elements in plagioclase and K-feldspar; only the outermost rims of plagioclase phenocrysts were used to calculate water contents by the Waters & Lange (2015) hygrometer.

Thermobarometry

Oxygen fugacity and water content were estimated from *rdm* hornblende compositions using the multiparameter calculator of Ridolfi *et al.* (2010); associated errors are ±0.4 log units and ±0.4 wt.%, respectively. As fractional crystallization of other phases and variations in melt water content may affect the temperature estimates (Erdmann *et al.*, 2014), temperatures were calculated using the mono-mineral thermometer of Putirka (2016), which has an uncertainty of ±30°C. The hornblende-plagioclase thermometer of Holland & Blundy (thermometer B, 1994) was also applied to three hornblende-plagioclase pairs (±40°C). The scarcity of melt inclusions in the *rdm* An$_{41–59}$ plagioclase precluded direct measurement of volatiles, so that pressure was estimated from hornblende using the amphibole-melt barometer of Putirka (2016). The barometer of Putirka (2016) requires the SiO_2, Al_2O_3, K_2O, Na_2O and P_2O_5 contents of the coexisting melt. We estimate the silica content of melt using the SiO_2 predictor of Putirka (2016). The other major element contents required for the barometer were obtained from postglacial lavas with similar silica contents to those predicted from hornblende compositions (*asd* for andesites, *dlp* for dacites and *rdcn* for rhyodacites; data from Hildreth *et al.*, 2010; Andersen *et al.*, 2017). As shown below, pressures calculated using the amphibole-melt barometer of Putirka (2016) are similar to those calculated by previous works (Andersen *et al.*, 2017 using amphibole-melt

barometer; Klug *et al.*, 2020 using volatile saturation pressure) despite the high uncertainty of the method (±200 MPa). The SiO_2 predictor of Putirka (2016) has an associated error of ±3.6 wt.% SiO_2 that increases the uncertainty of the amphibole-melt barometer up to ±300 MPa. Hornblende compositions used for geothermobarometry are provided in the Supplementary Material.

The plagioclase-glass hygrometer of Waters & Lange (2015) was applied to plagioclase outer rims of *rle* and *rln* samples using the Fe-Ti oxide temperatures of Andersen *et al.* (2017); the hygrometer is not sensitive to pressure and has an uncertainty of ±0.35 wt.%. Because of the scarcity of melt inclusions in the *rle* crystals, water saturation pressures were estimated using the method of Ghiorso & Gualda (2015) based on the calculated range of water contents and Fe-Ti oxide temperatures. Plagioclase and glass compositions used in the hygrometer and the water pressure saturation calculations are provided in the Supplementary Material.

RESULTS
Geochemistry

New analyses of groundmass glasses (Table 1 and Supplementary Material) are plotted together with whole-rock geochemistry of major and trace element data from Hildreth *et al.* (2010) and Andersen *et al.* (2017), melt inclusion glass in the *rdm* rhyolite (hosted in plagioclase and quartz), *rle* and *rln* rhyolites (plagioclase-hosted; Klug *et al.*, 2020) and groundmass glass in rhyodacites (Cáceres *et al.*, 2018). LdM products preserve an almost continuous whole-rock compositional range from 51 to 77 wt.% SiO_2 with a peak of total alkalis (~9.5 wt.% $Na_2O + K_2O$) at 74 wt.% SiO_2 (Fig. 3a). All eruptive products lie just below the boundary of alkaline and subalkaline series (Fig. 3a); mafic rocks (<62 wt.% SiO_2) lie in the calc-alkaline series and silicic products (>62 wt.% SiO_2) are high-K calc-alkaline (Fig. 3b). The *rdm* and *rle* magmas
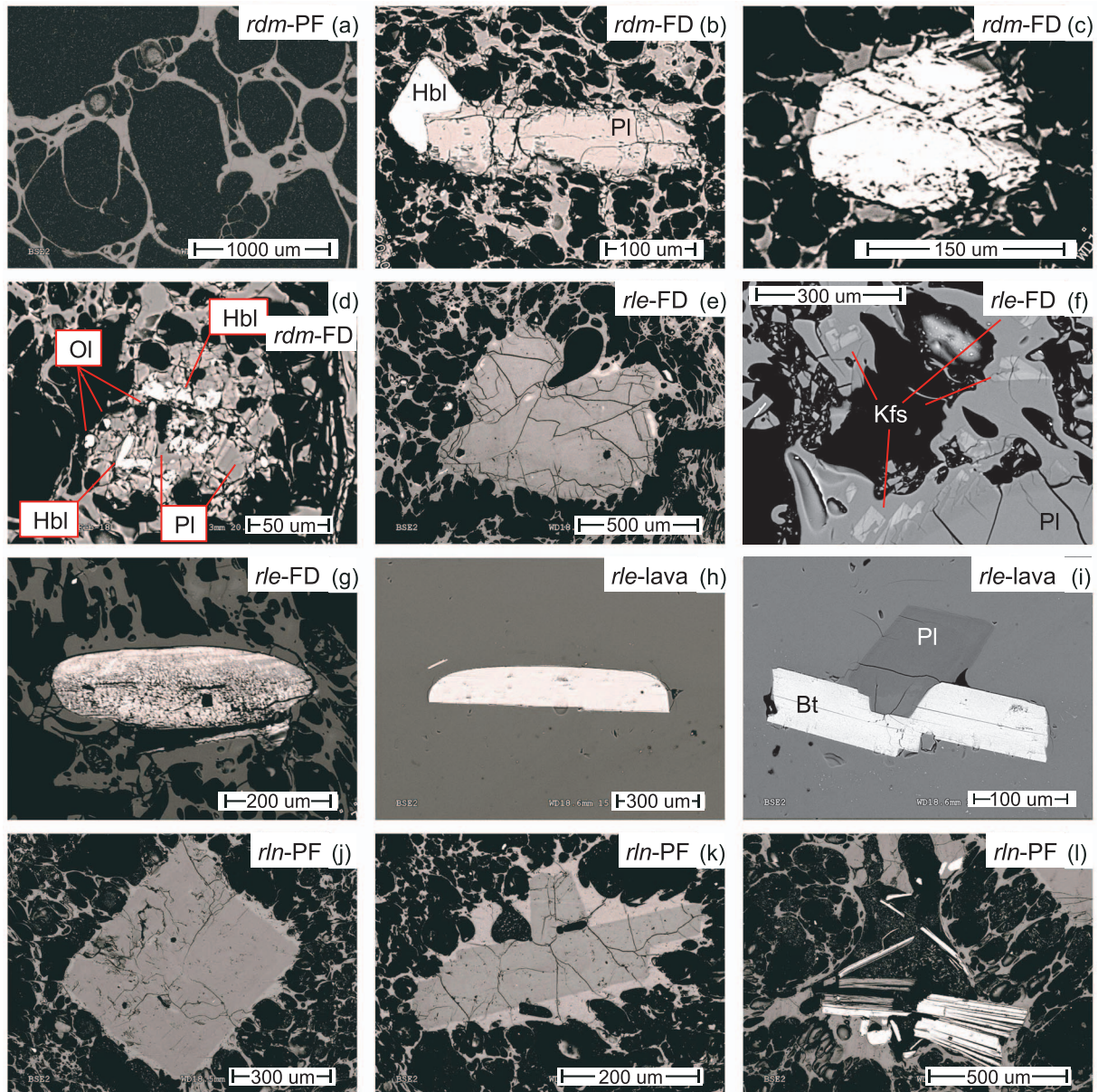
Fig. 4. General petrography of *rdm*, *rle* and *rln*. (a) An aphyric *rdm* pumice from sample site A1. (b) Crystal clot of plagioclase and hornblende. (c) Hornblende crystal. (d) Mafic blob with elongate plagioclase, olivine and hornblende crystals. (e) Plagioclase clot. (f) Plagioclase phenocryst with outer rim of K-feldspar. There are skeletal microcrysts of K-feldspar in groundmass. (g) Anhedral biotite phenocryst. (h) Subhedral biotite phenocryst. (i) Crystal clot of plagioclase and biotite. (j) Plagioclase phenocrysts. (k) Plagioclase clot. (l) Biotite crystals. All the pictures are BSE images. PF = Pyroclastic flow; FD = Fall deposit.

are some of the most silicic products of the LdM postglacial stage (76.7 and 75.7 wt.% SiO_2, respectively), whilst the *rln* is one of the most alkalic postglacial silicic magmas (73.4 wt.% SiO_2 and 8.98 wt.% $Na_2O + K_2O$).

The *rdm* and *rle* groundmass glasses (averages of ~77.0 and ~76.3 wt.% SiO_2, respectively) are similar to their corresponding whole-rock geochemistry, consistent with the low observed crystal content. In contrast, *rln* groundmass glasses are more evolved than the bulk composition (averages of ~75.3 wt.% SiO_2; Fig. 3a,b) because of the higher crystal content. In detail, groundmass glass compositional trends among *rdm* and *rle* eruptive products show a negative correlation of Na_2O with SiO_2; Na_2O and Al_2O_3 show no correlations with silica in *rln* glasses (Fig. 3c, d). Compatible elements FeO, MgO and CaO decrease with increasing SiO_2 (Fig. 3e, f); MgO variability reflects its very low concentration

($\leq$0.3 wt.%; Fig. 3f). Plagioclase-hosted melt inclusions of *rdm* have the lowest and most variable silica content (71.1–76.4 wt.%) among the rhyolites studied and follow the same compositional trends as the entire LdM suite. In contrast, quartz-hosted melt inclusions in *rdm* match the compositions found in the groundmass glasses. Plagioclase-hosted melt inclusion glasses of *rle* have slightly higher SiO_2 and lower Na_2O and Al_2O_3 than their corresponding groundmass glass geochemistry (Fig. 3c, d); plagioclase-hosted melt inclusions and groundmass glasses of *rln*, in contrast, have similar compositions.

Petrography

The three eruptions studied are aphyric to crystal-poor glomeroporphyritic rhyolites with glassy to microlite-bearing groundmasses. The rhyolites have mineral assemblages of plagioclase,
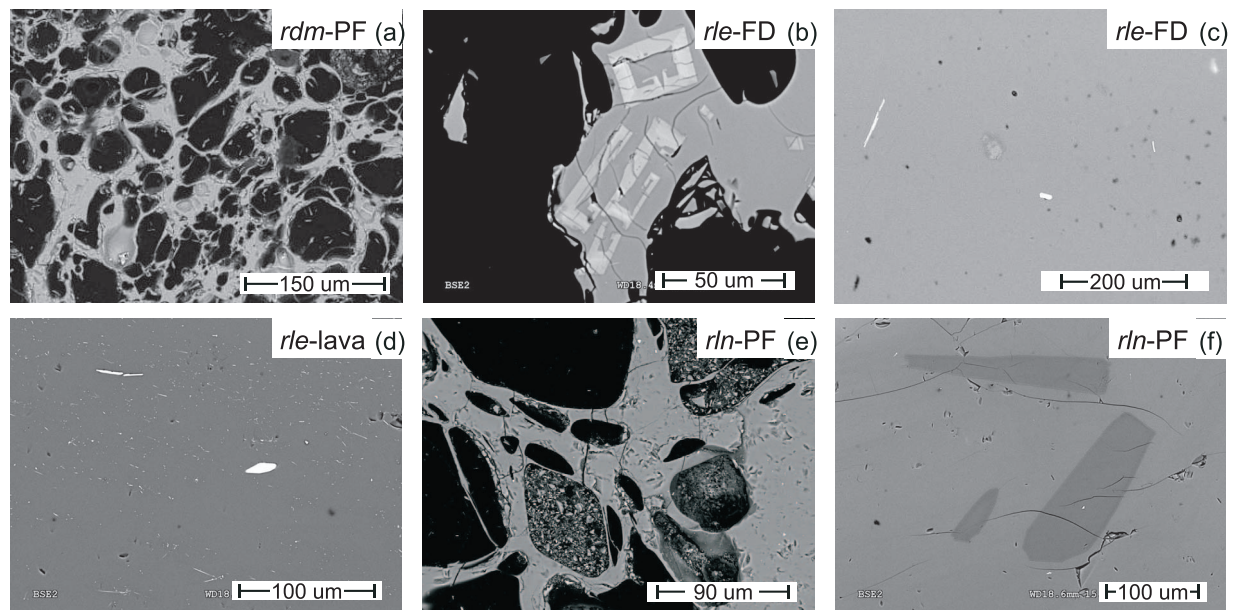
Fig. 5. Petrography of the groundmass of *rdm*, *rle* and *rln*. (a) Glassy groundmass of the *rdm* pumice clasts. (b) Skeletal K-feldspar microcrysts within the pumice groundmass. (c) Microcrysts of plagioclase, biotite and Fe-Ti oxides in an obsidian pyroclast. (d) Oriented microcrysts of biotite and Fe-Ti oxides in the *rle* lava flow. (e) Glassy groundmass of the *rln* pumice clasts. (f) Elongate plagioclase microcrysts in the obsidian juvenile clasts. All the pictures are BSE images. PF = Pyroclastic flow; FD = Fall deposit.

hornblende or biotite, Ti-magnetite, ilmenite, apatite and zircon in order of decreasing abundance (Table 2). Hornblende is exclusive to *rdm*; biotite occurs in all other crystal-bearing postglacial rhyolites. Glomerocrysts are common, formed by up to four plagioclase crystals and rarely associated with hornblende or biotite in the thin sections we examined. Plagioclase glomerocrysts have a common $An_{<20}$ outer rim. Juvenile pumice and lavas of *rle* and *rln* have similar mineralogy but vary in crystallinity.

The analyzed *rdm* pumice samples come from the late-erupted stratigraphy, which is characterized by the presence of mafic juvenile clasts, micrometric-to-centimetric mafic enclaves within the pumices, and granitoid lithics. Pumice clasts are highly vesicular (200–800 kg/m³; Fig. 4a) and almost aphyric, with ≤1% phenocrysts and no microcrysts in the groundmass (Fig. 5a). Plagioclase crystals are ≤0.3 mm long and anhedral to subhedral in form; they are either isolated or form mono- or polymineralic clots with hornblende (Fig. 4b). Hornblende crystals are 0.1 to 0.3 mm long, elongate and euhedral (Fig. 4c). The *rdm* pumices are the only LdM rhyolites that contain olivine and clinopyroxene crystals, which occur in crystal clots with plagioclase and hornblende within mafic blobs (Fig. 4d). The *rdm* granitoid lithics have quartz, two feldspars and both hornblende and biotite (Contreras-Hidalgo, 2020).

The *rle* pumice clasts are denser (~970 kg m⁻³) than *rdm* pumices and have 1% to 2% phenocrysts and 7–15% microcrysts in the groundmass. Pyroclastic obsidians and lavas are slightly more crystalline than the pumices (~3% phenocrysts and 12–20% microcrysts). All *rle* rock types have plagioclase crystals ≤1.8 mm-long that are either isolated or form clots (Fig. 4e), elongate biotite crystals 0.1 to 0.8 mm long and groundmass with microcrysts of feldspar and oxides. Crystal shapes, feldspar rim compositions and groundmass minerals, however, vary according to rock type. Pyroclast phenocrysts are anhedral-to-subhedral with rounded rims (Fig. 4e, g, h). In the pumice, K-feldspar forms both outer rims around plagioclase phenocrysts and clots (Fig. 4f) and microcrysts with skeletal textures (Fig. 5b). In the obsidian, albitic plagioclase

is the late-crystallizing phase. Obsidian lavas have euhedral phenocrysts and glomerocrysts (Fig. 4i) and groundmass with elongate plagioclase, biotite and oxide microcrysts arranged in bands with microvesicles (Fig. 5c, d).

The *rln* pumice clasts are less dense than *rle* pumice clasts (average density of ~800 kg m³) and have 6–13% phenocrysts and a glassy groundmass. The *rln* pyroclastic obsidians and lavas are slightly more crystalline than the pumices (~12–25% phenocrysts and 15–25% microcrysts in groundmass; Cáceres et al., 2018). Unlike *rle*, phenocryst textures do not vary according to eruption style. Plagioclase crystals are ≤3.0 mm-long, equant to slightly elongate, subhedral with rounded rims (Fig. 4j) and are surrounded by glass 10 to 50 μm thick (Fig. 4k). Crystal clots have growth rims of more albitic plagioclase. Biotite crystals are 0.1–3.5 mm long, more elongate than those of *rle* and mostly euhedral with regular rims (Fig. 4l). The pumice groundmass is aphyric (Fig. 5e), and the obsidian groundmass has elongate microlites of plagioclase (Fig. 5f).

Plagioclase chemistry

New analyses of major and minor elements in plagioclase crystals by EPMA are compared with major and minor element data from Andersen et al. (2018) by EMPA and LA-ICPMS (see details in Supplementary Material). For each rhyolite, plagioclase groups are determined according to An clusters (Fig. 6) or sharp variations in An versus minor element diagrams (Fig. 7 and Table 3). The modal anorthite contents of these plagioclase groups are used in MELTS simulations of storage and ascent conditions (Tables 4-9). Major and minor elements in hornblende, biotite and K-feldspar crystals are in Supplementary Material.

Plagioclase phenocrysts in our *rdm* samples are more anorthitic than those reported by Andersen et al. (2018). This discrepancy most likely reflects stratigraphic variations. Our analyses yield ~2/3 of the crystals with slight normal zoning ($An_{41–45}$; Fig. 6 and S1); the rest are normally zoned with cores of $An_{51–59}$ and outer rims of $An_{41–43}$. Data of Andersen et al. (2018), in contrast,
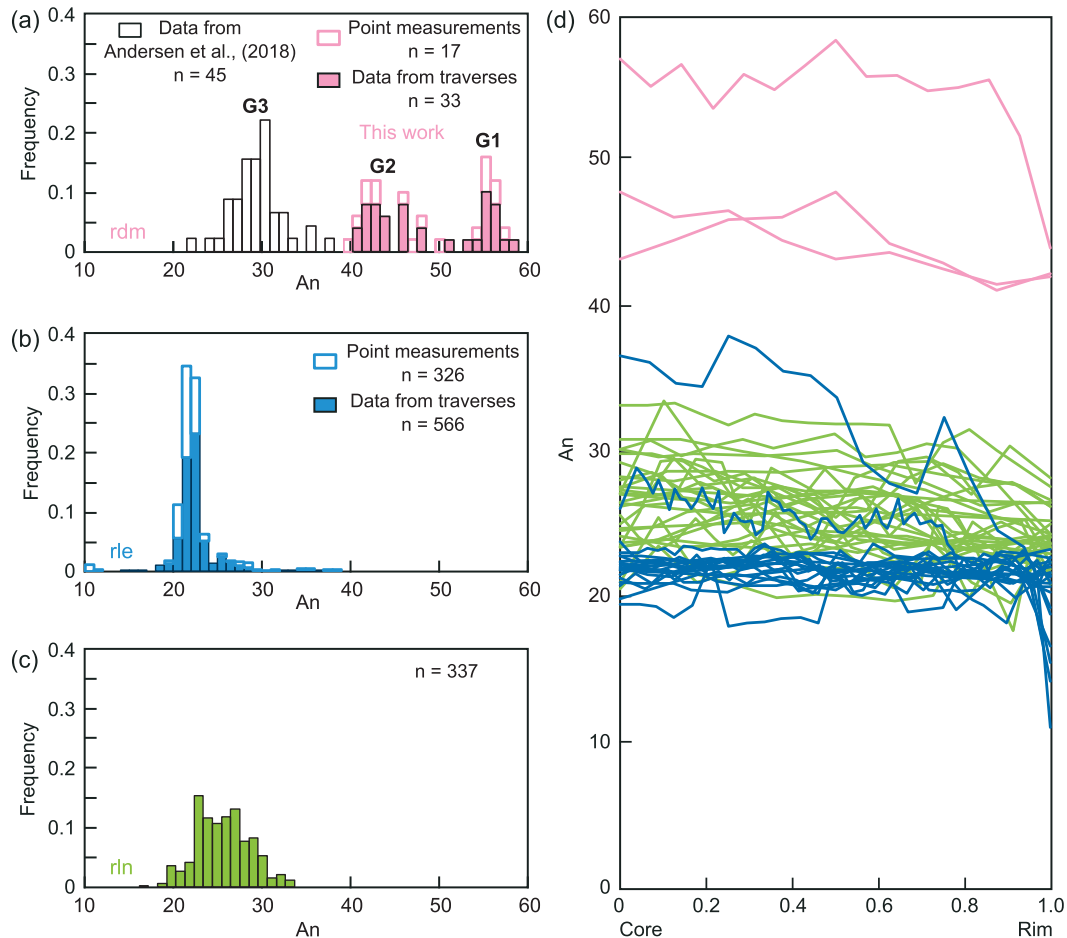
Fig. 6. Anorthite content of *rdm*, *rle* and *rln*. (a)-(c) Histograms of anorthite content from plagioclase traverses of *rdm* (a), *rle* (b), and *rln* (c). In (a), point analyses of plagioclase phenocrysts have been added from Andersen *et al.* (2018) and the three An modes are classified to facilitate discussion of plagioclase compositions and to relate these results to MELTS simulations reported in Figures 10 and 11. In (a) and (b), point analyses from additional crystals have been added to increase the data set. (d) Plagioclase traverses for the three rhyolites analyzed with position plotted non-dimensionally as location relative to the core and rim, regardless of the plagioclase size.

show a broad mode of An$_{28–34}$ with a tail of more anorthitic plagioclase (An$_{35–50}$) that represents the cores of a few plagioclase crystals with mantles of An$_{20–30}$. As a whole, the data show three compositional modes at ~An$_{32}$ (G3), ~An$_{44}$ (G2) and ~An$_{56}$ (G1) (Fig. 6a) corresponding to the cores of three *rdm* plagioclase groups. Minor and trace element data (Fig. 7 and Table 3) show that the An$_{28–34}$ plagioclase have slightly increasing Fe with An and limited ranges of both SrO and BaO. In contrast, both An$_{41–45}$ and An$_{51–59}$ plagioclase have an increasing FeO with An, variable SrO and very low BaO.

The *rle* plagioclase phenocrysts form two groups based on their core compositions: >90% are unzoned with cores of ~An$_{22–23}$; the rest are normally zoned and have oscillatory zoned cores of An$_{26–39}$ with irregular rims on the more anorthitic bands (Fig. 6 and S1). The data show a narrow compositional mode at ~An$_{22–23}$ and minor peaks at An$_{26–29}$ and An$_{12–17}$ (see also Andersen *et al.*, 2018; Cáceres *et al.*, 2018). The lowest An compositions are from the outer rims of crystals and microlites in obsidian. Analyses of An$_{33–39}$ represent digested inner cores (Fig. 6b); FeO and SrO (0.31–0.43 wt.% and 0.10–0.14 wt.%, respectively) increase and BaO (0.03–0.07 wt.%) decreases with increasing anorthite content (Fig. 7). FeO, SrO and BaO in unzoned An$_{22–23}$ plagioclase are variable with no clear trends (Fig. 7 and Table 3). The low An outer rims and microcrysts, in contrast, have high BaO.

Consistent with published data (Andersen *et al.*, 2018; Cáceres *et al.*, 2018), *rln* plagioclase compositions show a broad unimodal distribution of An$_{20–34}$ (Fig. 6c). All plagioclase phenocrysts have outer mantles of ~An$_{23–27}$ but can be classified into three groups based on differences in cores and inner mantle zones. ~60% of plagioclases are stepped-normal zoned with cores and mantles of ~An$_{27–33}$ (Fig. 5c). Each step shows slight oscillatory zoning (±1 An between minimum and maximum local values). ≥30% of plagioclase phenocrysts are slightly oscillatory zoned with a composition of ~An$_{25}$ (fluctuations ±2.5 An); ≤10% show oscillatory zoning with An$_{21–25}$. Only the obsidian pyroclasts and lava contain microlites with albitic (An$_{12–24}$) feldspar. With increasing An, FeO and SrO increase and BaO decreases (Fig. 7). For the same anorthite content, both FeO and SrO are higher in the *rln* plagioclase than in *rle* plagioclase (Table 3).

Thermobarometry

The results are organized by the minerals involved. Thermobarometry of *rdm* samples is used to determine the storage conditions (P–T–H$_2$O–fO$_2$) of magma forming amphibole together with plagioclase. Plagioclase-glass hygrometry methods are used to estimate water contents and water saturation pressures of *rle* and *rln* magmas using the compositions of the plagioclase phenocryst outer rims and groundmass glass and assuming they are in
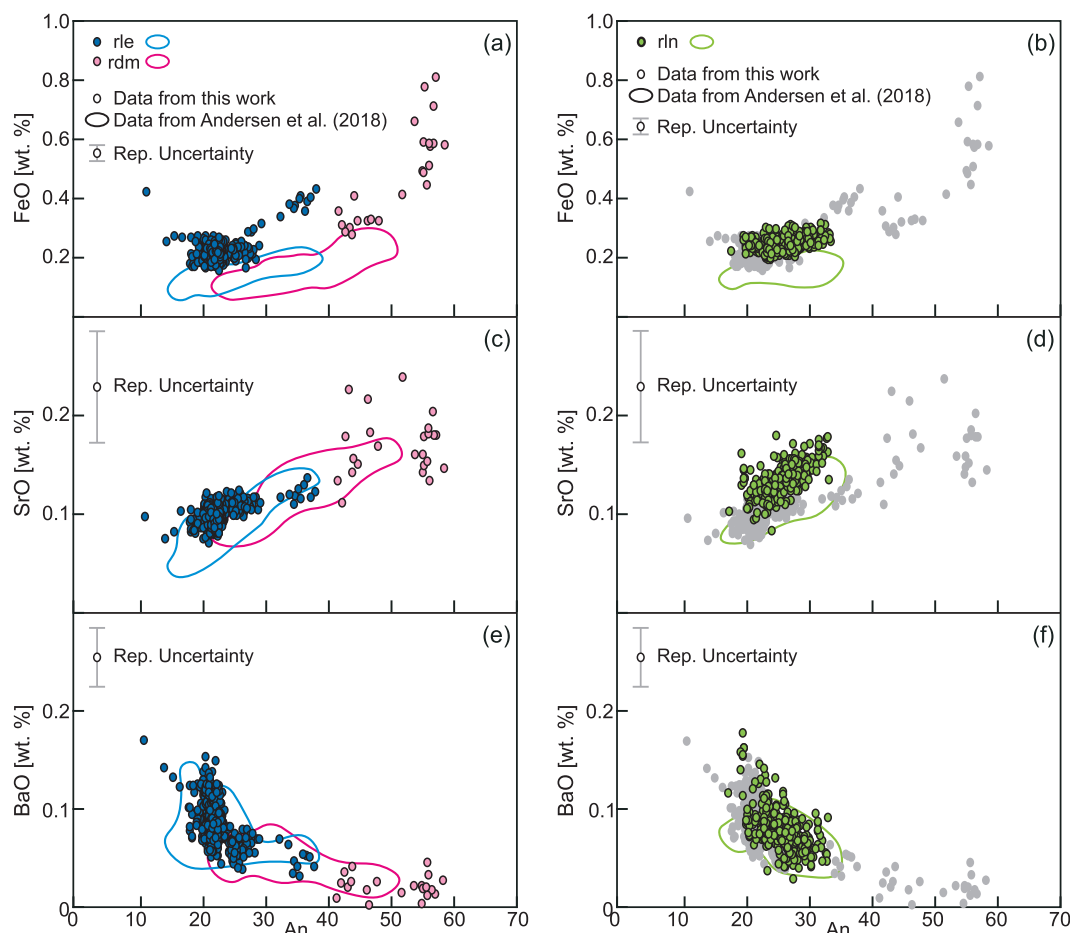
Fig. 7. Trace element composition in plagioclase. In (b), (d) and (f), grey dots are the same *rdm* and *rle* data highlighted in (a), (c) and (e). Symbol size is larger than bars representing the uncertainty for An contents ($\sigma_{An} = 0.086$).

equilibrium. A summary of estimated storage conditions can be found in Fig. 8. For details about calculations, see Supplementary Material.

Hornblende

Thermobarometry methods are applied to six amphibole core-rim pairs in the *rdm* pumices. The calculated silica content of a melt coexisting with the *rdm* amphibole (Putirka, 2016) shows that the hornblende crystals formed in three different intermediate magmas, all of which are less silicic than the high-silica rhyolite melt in which they were entrained. Temperature and pressure ranges estimated for amphibole formed in andesitic ($\sim$62.4 $\pm$ 3.6 wt% SiO_2) and dacitic magmas (63.9–65.4 $\pm$ 3.6 wt.% SiO_2) are 916–942 $\pm$ 30°C and 240–350 $\pm$ 300 MPa. Water contents and oxygen fugacities estimated using Ridolfi *et al.* (2010) are 4.9–5.8 $\pm$ 0.4 wt.% H_2O and 0.5–1.1 $\pm$ 0.4 ΔNNO, respectively. Temperature, pressure, and water content are negatively correlated with the silica content of the coexisting melt (Fig. 8a, b), whereas oxygen fugacity increases slightly with the silica content (Fig. 8c and Supplementary Material) and water content increases slightly with pressure (Fig. 8d). Hornblende from the most mafic melts was formed at higher pressures (300–350 $\pm$ 300 MPa), water contents (5.3–5.8 $\pm$ 0.4 wt.% H_2O) and temperatures ($\sim$940 $\pm$ 30°C) than those from intermediate magmas (240–300 $\pm$ 300 MPa, 4.9–5.3 $\pm$ 0.4 wt.% H_2O and 915–930 $\pm$ 30°C). Melt compositions calculated using hornblende rims form a second dacitic population (66.8–67.2 $\pm$ 3.6 wt.% SiO_2) at 170–220 $\pm$ 300 MPa (Fig. 8b).

The Holland & Blundy (1994) thermometer was applied to three hornblende-plagioclase pairs yielding an average temperature of 877 $\pm$ 40°C, slightly lower than estimates from amphibole alone.

Feldspars

The plagioclase-glass hygrometer of Waters & Lange (2015) was applied to plagioclase outer rims of the *rle* eruptive products (pumices, pyroclastic obsidians and lavas) and the *rln* pumice using two-oxide temperatures from Andersen *et al.* (2017). Water contents and water saturation pressures (P_{H2O}) of *rle* and *rln* are positively correlated (Fig. 8e), with *rle* plagioclase yielding higher H_2O (5.6–6.2 $\pm$ 0.35 wt.%) than *rln* (range of 5.1–5.6 $\pm$ 0.35 wt.%). The associated P_{H2O} ranges are, respectively, 193–229 MPa and 170–197 MPa, similar to the lowest hornblende crystallization pressures. The results are insensitive to subtle variations in temperature: an increment of 5°C decreases the calculated pressure by $\sim$0.5 MPa (Supplementary Material). Similarly, water contents of *rdm* using plagioclase rim compositions from Andersen *et al.* (2018) ranges 4.6–5.0 $\pm$ 0.35 wt.% with an associated P_{H2O} range of 162–203 MPa.

MELTS simulations: Equilibrium between melt compositions and mineral assemblages

We use rhyolite-MELTS (e.g. Gualda *et al.*, 2012; Bégué *et al.*, 2014) to simulate the storage and ascent conditions of the LdM rhyolitic magmas. Various magma compositions are used to determine the compositions of melts in equilibrium with the observed anorthite

Table 3: Characteristic ranges of anorthite contents and minor elements of the plagioclase groups classified for the *rdm*, *rle* and *rln* rhyolites

Pl group	An	FeO [wt.%]	SrO [wt.%]	BaO [wt.%]
Rhyolite of LdM (rdm)				
G1	51–59	0.40–0.80	0.13–0.24	<0.04
G2	41–45	0.17–0.35	0.11–0.22	<0.04
G3	28–34	0.10–0.17	0.08–0.10	0.04–0.05
Rhyolite of Los Espejos (rle)				
	22–23	0.16–0.28	0.08–0.13	0.04–0.17
Rhyolite of Las Nieblas (rln)				
	23–30	0.20–0.33	0.09–0.18	0.03–0.19

Table 4: Starting thermodynamics conditions and results using the corresponding rhyolitic magma compositions by MELTS software

Starting thermodynamic conditions

Pressure [MPa]			Temperature [°C]			Water content	Water saturation	Oxygen fugacity
P_{min}	P_{max}	ΔP	T_{min}	T_{max}	ΔT	[wt.%]	[wt.%]	ΔQFM
rdm simulations								
50	250	10	650	824	1	4.8	7.6	1
rle simulations								
50	250	10	650	847	1	5.8	7.6	2
rln simulations								
50	250	10	650	894	1	5.4	7.6	2

Saturation temperatures of some mineral phases and simulated An contents

Plagioclase saturation T [°C]		Quartz saturation T [°C]		K-feldspar saturation T [°C]		An content[1]	
T_{min}	T_{max}	T_{min}	T_{max}	T_{min}	T_{max}	Min	Max
rdm simulations[2]							
803	824	747	804	715	799	4	12
750	811	734	805	711	799	4	13
rle simulations[2]							
811	846	734	820	711	799	7	14
769	846	732	820	711	799	7	15
rln simulations[2]							
846	892	730	816	711	795	7	18
806	892	729	816	711	795	7	19

[1]At colder temperatures than the saturation temperatures of K-feldspar for *rdm* and quartz for *rle* and *rln*.
[2]The first row shows results using the water content measured by the plagioclase-glass hygrometer, and the second row shows results assuming water saturation.

contents in the LdM plagioclase. First, we use the corresponding whole-rock rhyolite compositions to determine if the An in plagioclase could form in rhyolitic magmas without quartz or K-feldspar. We then run simulations using three different intermediate magma compositions (62–68 wt.% SiO$_2$) to determine the origin of the most anorthitic (An$_{51–59}$) *rdm* plagioclase. For each rhyolitic and intermediate composition, we use a matrix of equilibrium conditions from liquidus to solidus temperatures and pressure increments of 10 MPa. Whether the bulk composition is appropriate is assessed by comparing the simulated An in plagioclase and major element compositions in melt with those observed in the LdM rhyolite samples. Adiabatic ascent conditions were simulated to assess crystallization (or disequilibrium) conditions of quartz (*rdm*), K-feldspar (*rle*) and biotite (*rle,rln*) and to analyze the potential role of magma temperature and decompression-driven crystallization in the eruption styles of the *rdm*, *rle* and *rln* rhyolites. A summary of starting conditions and results of MELTS simulations are in Figures 9-13 and Tables 4-9.

Equilibrium between rhyolite melts and plagioclase

The corresponding whole-rock compositions (Table 1) and the modal water contents calculated by the plagioclase-glass hygrometer (Table 4) are used to determine if the *rdm*, *rle* and *rln* plagioclase (Fig. 6 and Table 3) formed in rhyolite magma reservoirs. With these water contents, the rhyolite magmas are water undersaturated at ∼ > 150 MPa. Consistent with pressure ranges of the rhyolite batches within the silicic crystal mush recognized by geophysical imaging (e.g. Wespestad *et al.*, 2019; Cordell *et al.*, 2020), we use a pressure range of 50–250 MPa. Phase diagrams (Fig. 9a, b, c) show that plagioclase liquidus temperature > quartz liquidus temperature > K-feldspar liquidus temperature for each *rdm*, *rle* and *rln* magma composition. As the *rdm* samples do not have K-feldspar and the *rle* and *rln* samples lack quartz, we evaluate the simulated An contents in plagioclase only for temperatures higher than the liquidus temperatures of those phases. We find that modal plagioclase compositions in *rdm*, *rle* and *rln* cannot be simulated using their corresponding whole-rock rhyolite compositions. The

Table 5: Intermediate magma compositions and starting thermodynamics conditions used to model storage conditions by MELTS software

Magma compositions[1]									
SiO_2	TiO_2	Al_2O_3	$FeO*$	MnO	MgO	CaO	Na_2O	K_2O	P_2O_5
High-silica andesite									
62.5	1.066	16.7	5.27	0.111	2	4.63	4.71	2.64	0.395
Dacite									
64.1	0.87	16.86	4.16	0.11	1.61	3.89	4.89	2.76	0.35
Rhyodacite									
68.2	0.59	15.84	2.98	0.1	0.96	2.6	4.95	3.18	0.21

Starting thermodynamic conditions							
Pressure [MPa]			Temperature [°C]			Water content	Oxygen fugacity
P_{min}	P_{max}	ΔP	T_{min}	T_{max}	ΔT	[wt.%]	ΔQFM
High-silica andesite							
100	400	10	671	1025	1	5.5	1
Dacite							
100	400	10	677	1012	1	5.5	1
Rhyodacite							
100	400	10	650	1006	1	5.8	2

[1]Magma compositions for the high-silica andesite, the dacite and the rhyodacite correspond to the units *asd*, *dlp* and *rdcn* respectively. Whole-rock composition data were obtained by XRF from Andersen *et al.* (2017) and Hildreth *et al.* (2010).

Table 6: *rdm* plagioclase crystallization conditions obtained by MELTS software[1]

	$An_{51–59}$ + Hbl (G1)		$An_{41–45}$ + Hbl (G2)		$An_{28–34}$ (G3)[2]	
High-silica andesite						
$P^{[max-min]}$ [MPa][3]	350	300	300	240	220	160
$T^{[min-max]}$ [°C]	903–945	890–934	830–848	845–864	690–797 (708)	703–816 (713)
$SiO_2^{[Tmin-Tmax]}$ [wt.%]	67.7–65.5	67.4–64.5	70.5–69.4	70.4–69.1	73.4–73.8 (77.0)	74.7–73.6 (76.7)
$Cxs^{[Tmin-Tmax]}$ [%]	16–4	22–8	41–33	41–33	100–56 (69)	100–56 (70)
$H_2O^{[Tmin-Tmax]}$ [wt.%]	6.7–5.8	7.1–6.0	8.2–9.2	7.1–7.1	7.0–6.9 (6.5)	5.8–5.7 (5.5)
Dacite						
$P^{[max-min]}$ [MPa][3]			300	240	220	160
$T^{[min-max]}$ [°C]			868–897	861–888	748–831	774–853
$SiO_2^{[Tmin-Tmax]}$ [wt.%]			69.8–68.5	70.0–68.8	77.6–72.2	76.2–71.8
$Cxs^{[Tmin-Tmax]}$ [%]			25–17	25–18	57–40	57–40
$H_2O^{[Tmin-Tmax]}$ [wt.%]			6.2–6.9	6.9–6.3	6.5–6.6	5.4–5.4
Rhyodacite						
$P^{[max-min]}$ [MPa][3]					220	160
$T^{[min-max]}$ [°C]					827–863	848–876
$SiO_2^{[Tmin-Tmax]}$ [wt.%]					73.5–71.7	73.2–71.6
$Cxs^{[Tmin-Tmax]}$ [%]					21–10	21–11
$H_2O^{[Tmin-Tmax]}$ [wt.%]					6.5–6.1	5.4–5.3

[1]Range values of SiO_2, crystallinity (Cxs) and H_2O correspond to the minimum and the maximum temperature.
[2]In the case of the high-silica andesite, the values in parenthesis correspond to those where SiO_2 in melt is the maximum for the temperature range estimated.
[3]Selected pressure ranges are those calculated with Hbl barometer. For each magma composition, ranges of temperature, silica content, crystallinity and water content correspond to these pressure ranges. Figure 10 shows An contents for the whole pressure and temperature field simulated.

Table 7: *rle* and *rln* storage conditions obtained by MELTS software[1]

	rle ($An_{22–23}$ + Bt)		*rln* ($An_{23–30}$ ± Bt)[2]	
$P^{[max-min]}$ [MPa]	230	190	200	170
$T^{[min-max]}$ [°C]	773–794	783–805	793–845 (828)	803–857 (838)
$SiO_2^{[Tmin-Tmax]}$ [wt.%]	76.8–75.6	76.7–75.4	76.0–72.7 (73.7)	75.8–72.5 (73.5)
$Cxs^{[Tmin-Tmax]}$ [%]	39–33	39–33	36–17 (24)	35–17 (23)
$H_2O^{[Tmin-Tmax]}$ [wt.%]	6.6–6.6	5.9–5.9	6.1–6.1 (6.0)	5.5–5.5 (5.5)

[1]Similar to Table 6, the selected pressure ranges are those calculated with plagioclase-glass hygrometer and the other parameters correspond to these pressure ranges. Figure 12 shows An contents for the whole pressure and temperature field simulated.
[2]The values in parenthesis correspond to the biotite liquidus temperature.

highest An that the *rdm*, *rle* and *rln* magmas would form are 12, 14, and 18 respectively (Table 4), significantly lower than those measured in the cores and mantles of *rdm*, *rle* and *rln* plagioclase phenocrysts, but consistent with the albitic phenocryst outer rims and microlites (Fig. 6 and Table 3). An>20 is simulated at >220 MPa but at temperatures lower than

Table 8: Starting compositions and thermodynamics conditions used to simulate adiabatic fractional crystallization for ascent conditions by MELTS software

Starting compositions

SiO$_2$	TiO$_2$	Al$_2$O$_3$	Fe$_2$O$_3$	FeO	MnO	MgO	CaO	Na$_2$O	K$_2$O	P$_2$O$_5$
rdm ascent simulations starting at 160 MPa[1]										
76.97	0.25	11.97	0.25	0.3	0.15	0.57	1.36	3.01	4.85	0.32
rdm ascent simulations starting at 220 MPa[1]										
77.22	0.21	11.93	0.23	0.27	0.16	0.45	1.36	2.99	4.86	0.33
rle explosive ascent simulations[2]										
76.67	0.24	12.2	0.25	0.3	0.15	0.55	1.38	3.18	4.77	0.31
rle effusive ascent simulations[2]										
75.39	0.26	12.91	0.29	0.37	0.14	0.71	1.44	3.68	4.51	0.29
rln effusive ascent simulations[2]										
75.79	0.27	12.65	0.29	0.35	0.14	0.7	1.42	3.49	4.61	0.3

Thermodynamic conditions

	Pressure [MPa]			Temperature [°C]	Water content [wt.%]
P$_i$	P$_f$		ΔP	T$_i$[3]	H$_2$O$_i$
rdm ascent simulations starting at 160 MPa					
160	90		5	784	5.34
rdm ascent simulations starting at 220 MPa					
220	90		5	767	6.38
rle explosive ascent simulations					
190	20		5	783	5.9
rle effusive ascent simulations					
190	20		5	805	5.93
rln effusive ascent simulations					
170	20		5	819	5.55

[1]The starting compositions and water contents are those of the melt composition simulated at the minimum temperature for the *rdm* rhyolite.
[2]The starting compositions and water contents are those of the melt composition simulated at the minimum pressure for the corresponding rhyolite.
[3]The initial temperatures are within the ranges simulated for the storage conditions.

Table 9: Temperature ranges, mass percent of crystallization and feldspar composition during the *rdm* subsurface ascent and the *rle* explosive and effusive and *rln* effusive eruption ascent obtained from simulations of adiabatic fractional crystallization using MELTS software. The mass weight percent corresponds to the groundmass, not to the whole rock

	rdm from 160 MPa	*rdm* from 220 MPa	*rle* explosive	*rle* effusive	*rln* effusive
Temperature [°C]	784–788	765–772	775–787	802–812	819–828
Quartz [wt.%]	0	2.7	Suppressed	Suppressed	Suppressed
Plagioclase [wt.%]	6.1	10.6	14.9	24.5	23.8
An in plagioclase	16–20	14–18	8–21	5–23	7–24
K-Feldspar [wt.%]	0	0	6.5	0	0
Or in K-feldspar			46–64		
Biotite [wt.%]	0	0	0.9	1.4	1.9
Rhm-oxide and/or Spinel [wt.%]	<0.1	<0.1	<0.1	<0.1	<0.1
Total [wt.%]	6.3	13.6	22.4	25.9	25.7

the K-feldspar liquidus temperature and close to the solidus temperature.

Simulations using water-saturated rhyolite magmas for the entire pressure range (H$_2$O > 7.6 wt.%) show a lower plagioclase liquidus temperature at >150 Mpa and a subtle increase of the maximum An (Fig. 9d, e, f and Table 4) that, however, is not enough to reproduce the anorthite content of the dominant populations of *rdm*, *rle* and *rln* plagioclases.

Storage conditions of the Plinian-ignimbrite rdm magmas

To simulate the *rdm* storage conditions, we use the compositions of three available LdM postglacial intermediate (andesitic to rhyo-dacitic) samples because less evolved (than rhyolite) magma compositions are required to form higher anorthite contents (Fig. 6 and Andersen *et al.*, 2018). The samples were selected based on

comparison with SiO$_2$ calculated using the Hbl chemometer (Fig. 7 and Table 5). The matrix of equilibrium conditions simulated considers higher pressures (100–400 MPa) and higher magma liquidus temperatures (>1005°C) than those used for the rhyolite compositions. Simulated modal anorthite contents in plagioclase and magma crystallinity are compared to those observed in the *rdm* juvenile clasts. Simulation of the plagioclase-hornblende mineral assemblage would be more precise to assess the storage conditions of *rdm*, however, MELTS does not accurately predict hornblende saturation for wet intermediate to silicic magma compositions due to the lack of thermodynamic models for hydrous mafic silicates (Gualda *et al.*, 2012). Andersen *et al.* (2017) indicate that the crystallization of LdM amphibole (SiO2/MgO = 2.6–3.4) would have a similar impact on the magma SiO$_2$/MgO ratio to the crystallization of two pyroxenes (SiO$_2$/MgO = 2–3 and 3.3–4.4 for
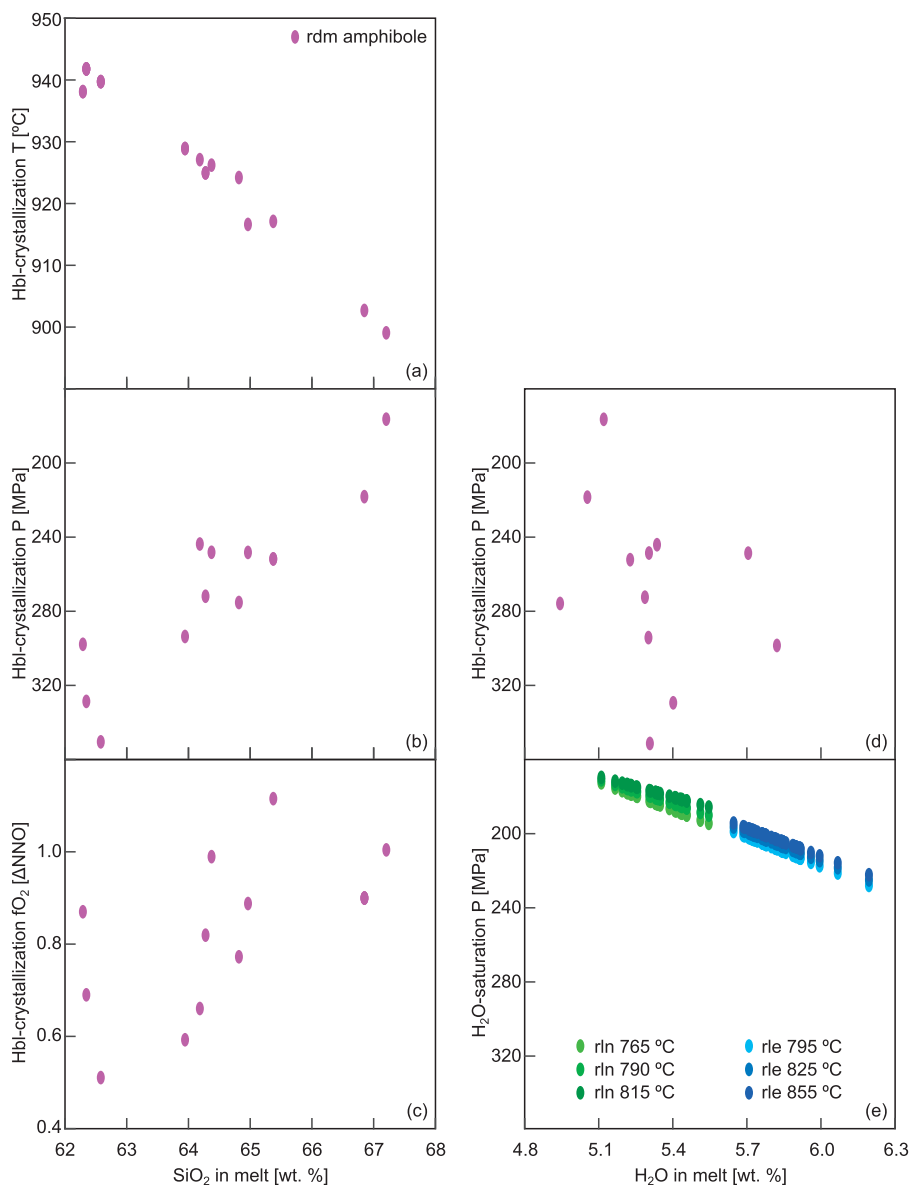
Fig. 8. Geothermobarometry. Putirka (2016) thermometry, barometry and chemometry in (a) and (b) and Ridolfi *et al.* (2010) oxybarometry and hygrometry in (c) and (d) were applied to compositions of amphiboles from *rdm* pumice clasts. (e) Water saturation pressure and water content were estimated at three temperatures by Ghiorso & Gualda (2015) H_2O-CO_2 saturation pressure calculator and Waters & Lange (2015) plagioclase-glass hygrometer, respectively, for plagioclase-melt pairs of *rle* and *rln*. Uncertainties have not been added to the figure because of the large error bars for pressure values make the plots hard to follow; the associated uncertainties are: P = ±300 MPa, T = ±30°C, fO_2 = ±0.4 log units, H_2O = ±0.4 and ±0.35 wt.% (Ridolfi *et al.*, 2010 and Waters & Lange, 2015, respectively), SiO_2 in melt = ±3.6 wt.%.

Opx and Cpx, respectively) predicted by MELTS. Consequently, we replace hornblende by crystallization of orthopyroxene to approximate the evolution of the silica content in melt (e.g. Gualda *et al.*, 2012; Andersen *et al.*, 2017).

The simulation outputs are used to construct pressure–temperature fields of An content in plagioclase, silica content in melt and magma crystallinity (Fig. 10 and Table 6). For the three magma compositions, plagioclase liquidus temperature > biotite liquidus temperature > quartz liquidus temperature > K-feldspar liquidus temperature; the liquidus temperature of orthopyroxene (proxy for hornblende) varies with the magma composition. Herein, we describe the predicted temperature, melt silica content, crystallinity and water content at pressure ranges calculated by Hbl and Pl-glass hygrometers (Tables 6 and 7). Figure 10 shows the simulated liquidus temperatures of mineral

phases, melt silica content and crystallinity for the whole pressure range simulated (100–400 MPa).

In the high-silica andesite, plagioclase and orthopyroxene (hornblende) start to crystallize together at ~955°C. The most anorthitic *rdm* plagioclase compositions (G1; An_{51-59}) are simulated at 890°C to 945°C, with a coexisting dacitic melt and at nearly water saturated conditions (Table 6). The phase diagram suggests that the G1 plagioclase-hornblende mineral assemblage formed without biotite and with a magma crystallinity <22% (Fig. 10a,d). Although simulations using the high-silica andesitic magma can reproduce the *rdm* G2 and G3 plagioclase, the simulated magma crystallinity is much higher than the crystallinity of the *rdm* samples (33–41% crystals for G2 plagioclase and 53% to 100% crystals for G3 plagioclase; Table 6); the latter would not be eruptible. Continued cooling causes quartz to crystallize,
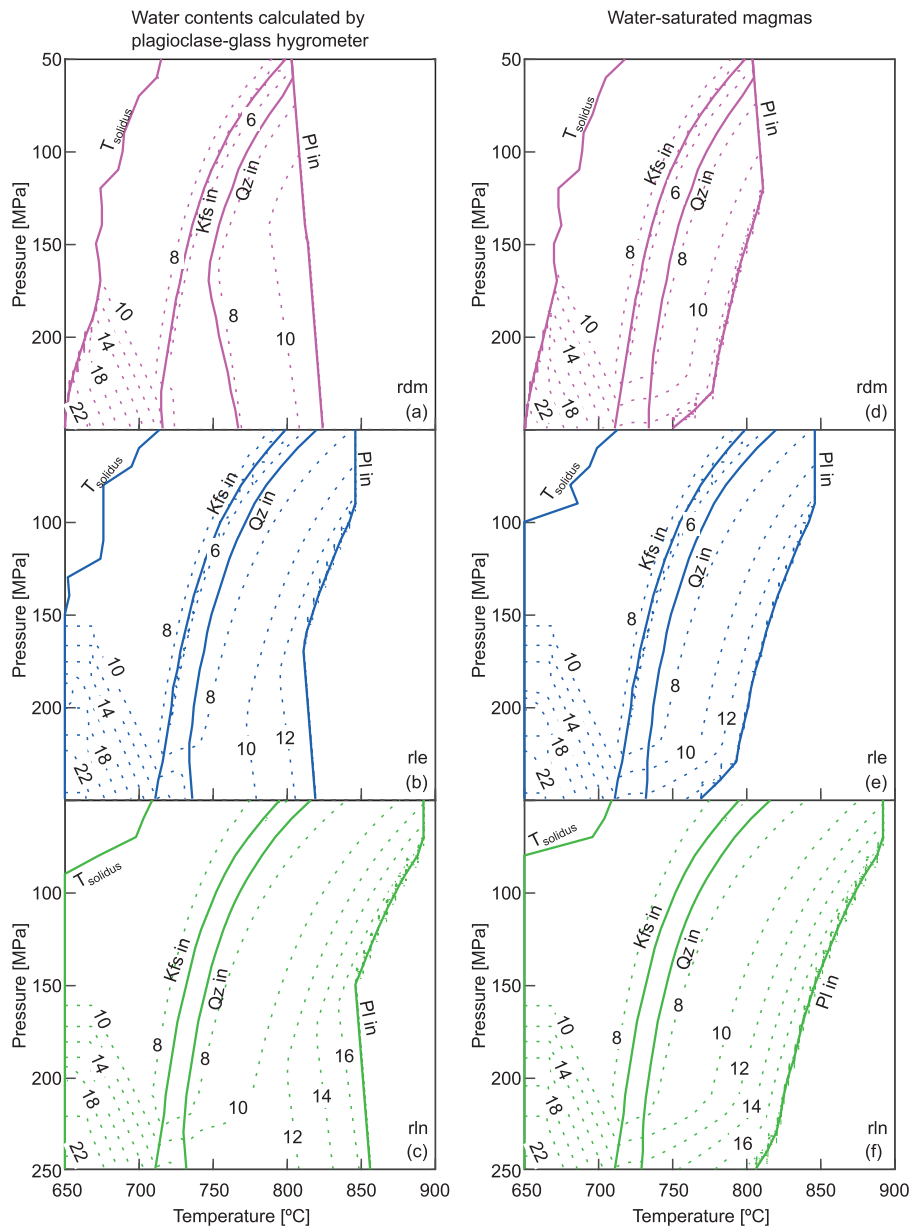
Fig. 9. Phase diagrams of quartz, plagioclase, and K-feldspar and anorthite contents in plagioclase obtained by MELTS simulations using the whole-rock compositions of the *rdm*, *rle*, and *rln* rhyolites (Table 1). (a)-(b)-(c) show MELTS simulations using the modal water contents obtained by plagioclase-glass hygrometry (Table 5) and (d)-(e)-(f) the same for water saturated conditions. Dashed lines are An content contours in integer intervals; some An values are labeled in black.

accompanied by a decrease in SiO_2. Under these near-eutectic conditions, the simulated magma crystallinity increases from 70% to 100% with cooling of only 15°C (from ~710°C to 695°C). The simulated mineral assemblage includes An_{28-29} plagioclase, hornblende (approximated by orthopyroxene), biotite, quartz, K-feldspar and apatite, which is similar to the mineralogy observed in the granitoid lithics.

In the dacite, plagioclase starts to crystallize at ~948°C and orthopyroxene (proxy for hornblende) at ~918°C. The G1 plagioclase cannot be reproduced with a dacitic magma. G2 plagioclase crystals (An_{41-45}) form at 861–897°C together with orthopyroxene (hornblende) and without biotite (Fig. 10b); the coexisting melt is rhyodacitic (68.5–70.0 wt.% SiO_2; Table 6) and the total crystallinity is 17–25% (Fig. 10e). Interestingly, G3 plagioclase (An_{28-34}) is simulated at 748–853°C, with a coexisting melt of 71.8% to 77.6 wt.% SiO_2 and a total crystallinity of 40% to 57% (Table 6);

however, it crystallizes together with biotite which is not observed in the *rdm* juvenile samples.

Unlike the G2 assemblage, the modal G3 *rdm* plagioclase (An_{28-34}) can also form in a rhyodacitic magma, without a mafic hydrous phase and at temperatures of 828°C to 876°C (Fig. 10c). Here the interstitial melt has a composition of rhyodacite to low-silica rhyolite (71.6–73.5 wt.% SiO_2) and a total crystallinity of 10% to 21% (Fig. 10f). Importantly, continued cooling causes the least anorthitic *rdm* plagioclase (An_{20-28}) to crystallize at 750°C to 760°C without quartz (Fig. 10c).

Storage conditions of *rle* and *rln* magmas

Although successful for reproducing the *rdm* phase assemblage, simulations that use high-silica andesitic and dacitic magmas cannot reproduce the *rle* and *rln* rhyolites, which require a lower
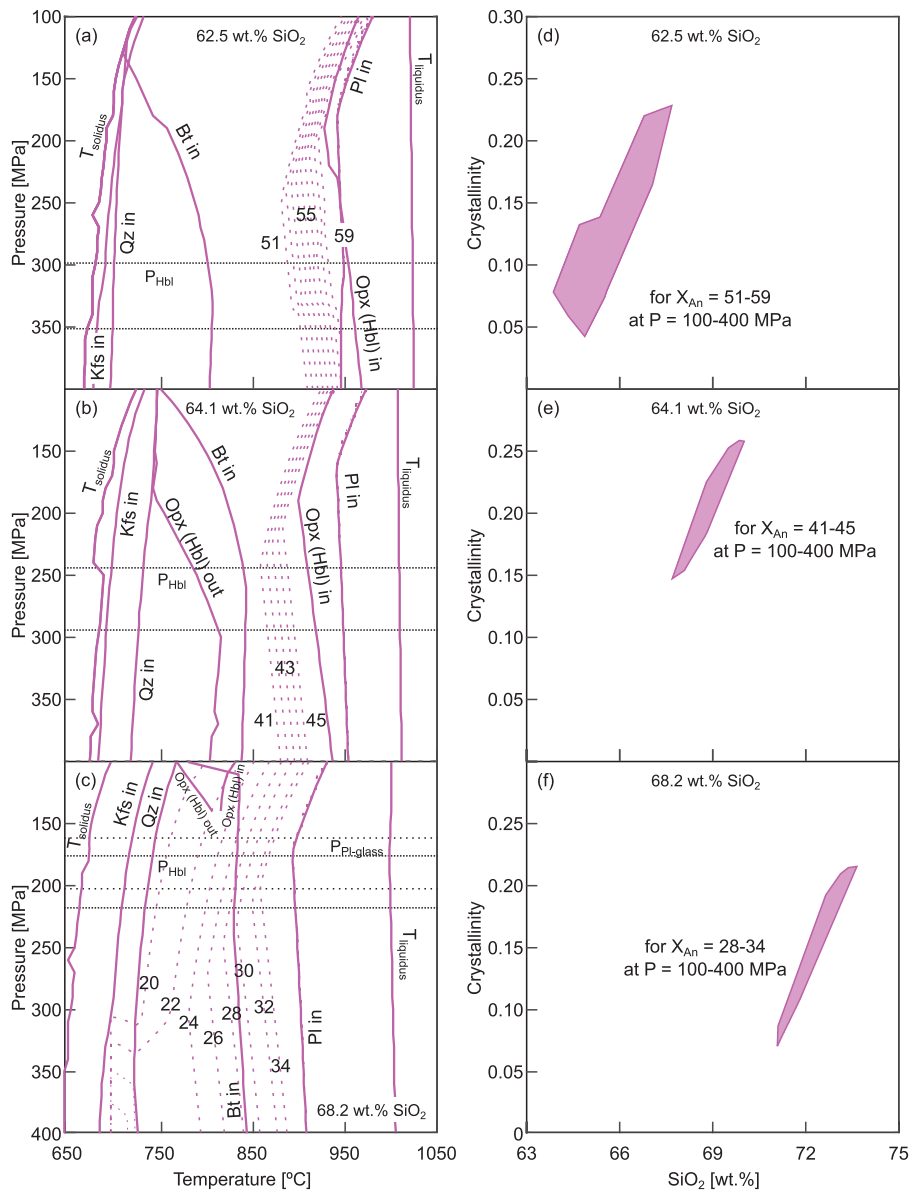
Fig. 10. Phase diagrams and P–T conditions to form the Plinian-ignimbrite of LdM (*rdm*) obtained by MELTS simulations. (a)-(b)-(c) show phase diagrams and An content contours and (d)-(e)-(f) show the magma crystallinity and silica content in melt forming the three *rdm* plagioclase groups (G1: An$_{51–59}$; G2: An$_{41–45}$; G3: An$_{28–34}$). Magma compositions used are a high-silica andesite (a)-(d), a dacite (b)-(e), and a rhyodacite (c)-(f). The whole-rock major element compositions of the three magma compositions are in Table 5. Dashed lines are An content contours in integer intervals of G1 in (a), G2 in (b) and G3 in (b) and (c). In (a)-(b)-(c) dotted lines are pressure ranges obtained from hornblende barometry and water saturation pressures.

An content in plagioclase and biotite not associated with K-feldspar or quartz. In contrast, simulations that use a rhyodacitic magma composition can form plagioclase of An$_{20–30}$ at similar temperatures obtained by two-oxide thermometry (Andersen *et al.*, 2017). On the basis of the above constraints, we use the bulk composition of the rhyodacite of Colada del Noroeste (*rdcn*; Fig. 1), one of the best-characterized postglacial rhyodacites of the LdM volcanic complex (e.g. Andersen *et al.*, 2018; Cáceres *et al.*, 2018), as the magma composition for MELTS modeling; this composition was also used to reproduce the *rdm* G3 plagioclase. The simulated phase diagram (Fig. 11a) shows a plagioclase liquidus temperature of ∼900°C at P = 170–230 MPa. The biotite liquidus is reached at ∼835°C. Quartz and K-feldspar liquidus temperatures are <750°C and decrease with pressure.

Our simulations show that the subplinian rhyolitic magmas formed far from the saturation of quartz and K-feldspar. An$_{22–23}$ plagioclase (>90% of *rle* feldspars) is simulated at 772°C to 805°C together with biotite (Fig. 11a and Table 7). The melt composition is 75.4–76.8 wt.% SiO$_2$; the magma contains ∼35% crystals (Fig. 11b) and is water saturated (5.9–6.6 wt.% H$_2$O; Fig. 11c). Plagioclase phenocrysts in the *rln* magma, in contrast, commonly have cores of An$_{26–30}$ that require higher temperatures (819–857°C) and slightly lower crystallinity and melt silica content than in the *rle* reservoir (Fig. 11b and Table 7). The dominant plagioclase composition (An$_{23–27}$) is simulated under cooler conditions (793–841°C), always below the biotite liquidus temperature of ∼828°C to 838°C and with a melt composition similar to that observed in the groundmass glasses; the water content (5.5–6.1 wt.%) is slightly lower, but overlaps with, that simulated for *rle* (Fig. 11c).
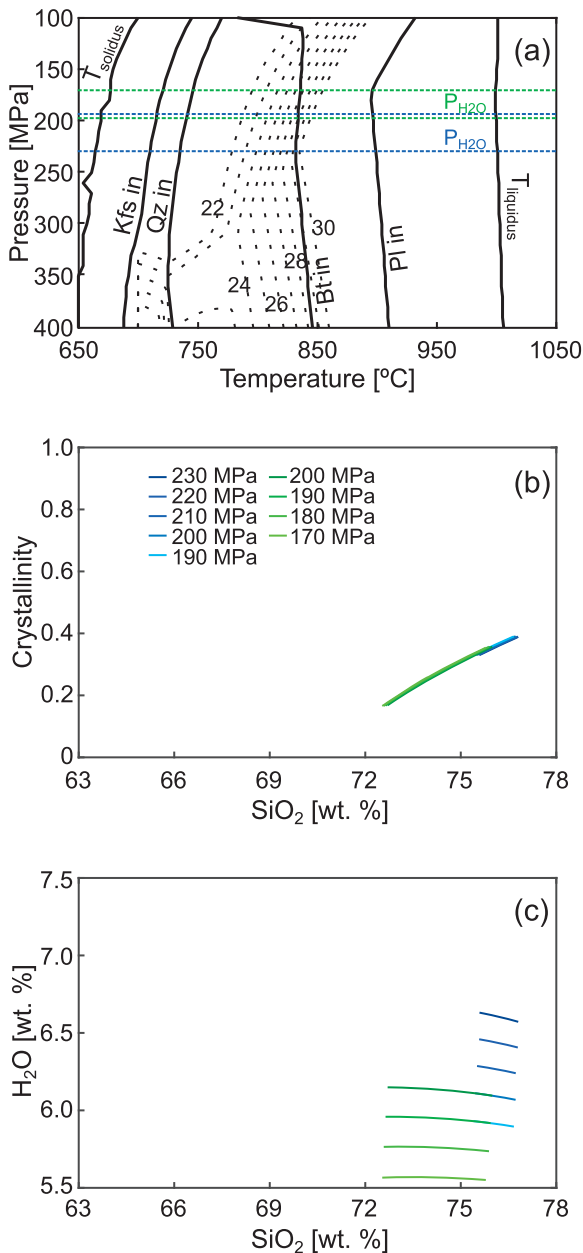
Fig. 11. Phase diagrams and P–T conditions to form the subplinian-effusive *rle* and *rln* eruptions obtained by MELTS simulations. (a) Phase diagram of *rle* and *rln* using a rhyodacitic magma composition and showing contours of An contents with dashed lines (*rle*: An$_{22-23}$; *rln*: An$_{23-30}$); pressures of *rle* (in blue) and *rln* (in green) are obtained from water saturation pressure. (b) Evolution of the crystallinity with silica content for different isobaric paths. Crystallinity is nearly independent of pressure for the range of potential storage pressures. (c) Evolution of the water content with silica content for the isobaric paths shown in (b).

Decompression-driven quartz crystallization in the rdm rhyolite magma

MELTS simulations using a rhyodacitic magma can reproduce the *rdm* An$_{20-34}$ plagioclase but do not predict quartz nor exceed 76 wt.% SiO$_2$ in the melt. As quartz-hosted melt inclusions suggest that quartz crystallized at 90–160 MPa (Klug *et al.*, 2020), we model rhyolite magma ascent in this pressure range to assess the conditions governing both quartz crystallization and the high-silica content (>77 wt.% SiO$_2$) of the *rdm* pumice clasts. We model magma ascent as adiabatic with decrements of 5 MPa and either

equilibrium or fractional crystallization. The oxygen fugacity is not buffered as it may vary with variations of water content and depressurization during ascent (Matjuschkin *et al.*, 2015).

To assess the influence of storage conditions on quartz crystallization, we simulate fractional crystallization P–T ascent paths starting from 160 and 220 MPa, which correspond to the minimum and maximum pressures calculated by the Hbl and Pl-glass hygrometers (Table 8). For each starting pressure, we use starting temperatures within the range simulated to reproduce An$_{20-34}$ plagioclase in the rhyodacite reservoir. For both starting pressures, plagioclase is the dominant phase (6–11%) and temperatures decrease slightly (−<1 Δ°C) and then increase (+4 Δ°C) at relatively high pressures (∼140 MPa; Fig. 12). The ascent paths from 160 MPa can crystallize An$_{16-20}$ plagioclase but cannot reproduce quartz. The ascent paths from 220 MPa and < 790°C can, in contrast, crystallize <3% of quartz together with An$_{14-18}$ plagioclase at <155 MPa (Fig. 12 and Table 9).

Ascent conditions of rle and rln magmas

Here we use the groundmass features of pumice and obsidian lavas to assess the conditions governing the explosive and effusive behavior of the post-*rdm* rhyolites. As the *rln* pumice clasts lack microcrysts, we model ascent conditions only for the *rln* effusive phase. We apply the same pressure decrements and oxygen fugacity as for *rdm* decompression. Simulations are quartz-suppressed because both *rle* and *rln* groundmasses lack quartz, although both rhyolite magmas should have reached quartz saturation during ascent; this suggests that quartz crystallization was limited by sluggish kinetics (Gualda *et al.*, 2012).

To assess the influence of storage conditions on the *rle* eruptions, we simulate two P–T ascent paths from 190 MPa using 783°C (explosive) and 805°C (effusive) as starting conditions; these correspond to the minimum and maximum temperatures simulated at the lowest magma reservoir pressure (Table 8). Although both equilibrium and fractional crystallization simulations produce similar results, the latter provide a better match with the groundmass mineralogy and crystallinity observed in the natural samples. Temperatures increase slightly (∼+6 Δ°C) and then decrease (∼−12 Δ°C) at low pressures (<∼ 50 MPa; Fig. 13). Crystallization associated with both P–T ascent paths is dominated by plagioclase; paths differ in the pressure at which biotite stops crystallizing, in the onset of K-feldspar crystallization, and in the total crystallinity achieved. In the colder ascent path, biotite stops forming at 100 MPa, 6% of Or$_{46-64}$ K-feldspar is formed after An$_{8-21}$ plagioclase, and 22% crystals are produced; in the hotter ascent path, biotite crystallization stops at 60 MPa, K-feldspar does not crystallize, and 25% crystals are formed (Fig. 13 and Table 9).

The *rln* effusive phase is simulated starting at 820°C and 170 MPa (Table 7). Decompression produces similar results to those of *rle* effusion (Fig. 13 and Table 9), with a crystallinity of ∼26% consisting primarily of An$_{10-24}$ plagioclase that become more albitic at lower pressures but not K-feldspar. Biotite stops crystallizing at 30 MPa.

DISCUSSION

Here we integrate whole-rock and mineral compositions, geothermobarometry and MELTS simulations to assess the storage and ascent conditions of the LdM rhyolites and their relation to the diverse eruptive styles. Table 10 contrasts the storage and ascent conditions of the *rdm*, *rle* and *rln* rhyolites, and summarizes their key petrological features revealing their differing eruptive styles.
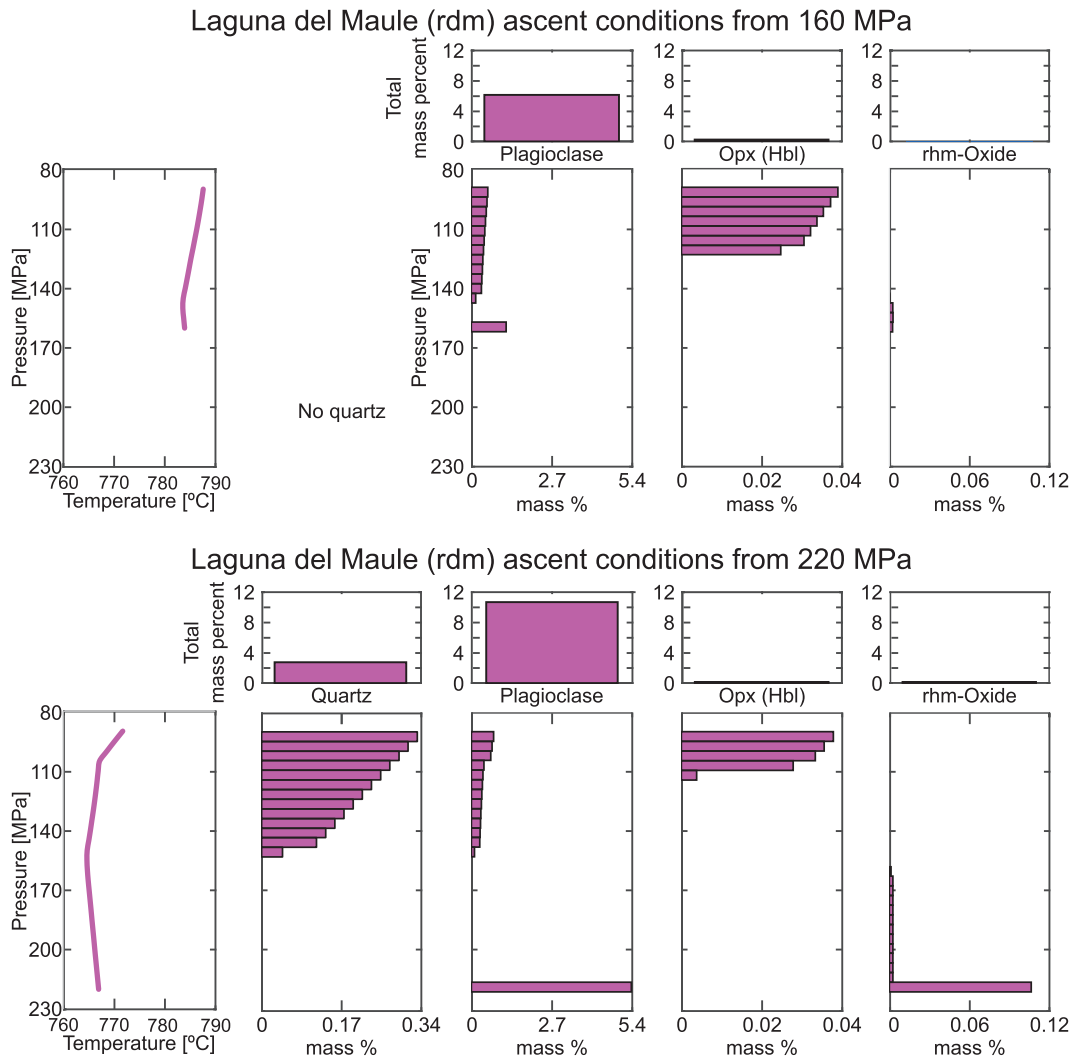
Fig. 12. Numerical simulations by MELTS of the ascent conditions forming quartz in the *rdm* magmas. The suggested P–T paths consider information from adiabatic fractional crystallization for two scenarios of starting pressure conditions. The wide vertical bars show the mass percent of quartz, plagioclase, orthopyroxene and rhm-oxide formed during ascent. Horizontal bars show crystallization per pressure interval (5 MPa). Crystallization of quartz occurs only when magma ascent starts at >220 MPa.

Storage and eruption conditions of the Plinian-ignimbrite *rdm* rhyolite

The largest LdM postglacial eruption (*rdm*) formed pyroclastic fall and flow deposits of >17 km^3 DRE and preceded the smaller rhyolites (Fierstein, 2018; Gho et al., 2019). The *rdm* deposits are unique in having not only low-density, high-silica pumice clasts and rare quartz phenocrysts but also mafic blobs and granitoid lithics, as well as An-rich plagioclase and hornblende (Hildreth et al., 2010; Fierstein, 2018; Fig. 4). Melt inclusions of basaltic to rhyolitic composition (Klug et al., 2020) indicate the presence of a mafic parental magma and a complex magma evolution. The lack of sharp intracrystal variations in anorthite content (Fig. 6) suggests that the three plagioclase groups formed in magma reservoirs of different compositions. Our applications of hornblende barometry, hornblende chemometry and MELTS simulations show that *rdm* magmas formed in at least three magma reservoirs and by two crystallization stages in a vertically extensive (90–350 MPa) magma plumbing system. Crystallization of An$_{51-59}$ plagioclase and hornblende crystals without strong disequilibrium textures (Fig. 4) requires ∼22% crystallization at high pressures (300–350 MPa) and temperatures (890–945°C) from a water-rich

(>5.3 wt.%), high-silica andesite (∼62 wt.% SiO$_2$) parental magma (Fig. 10a). The observed An$_{41-45}$ plagioclase-hornblende assemblage, in contrast, requires a crystal-poor dacitic magma at 240–300 MPa (Fig. 10b). Two scenarios can reproduce the An$_{28-34}$ plagioclase population: (1) continued cooling of the dacitic magma to a minimum of 750°C to form a crystal-rich (40–57% crystals) magma reservoir with interstitial melt of 72–78 wt.% SiO$_2$ or (2) crystallization in a hotter (827–876°C) crystal-poor rhyodacitic magma reservoir with rhyolitic melt (71.5–73.5 wt.% SiO$_2$) at 160 to 220 MPa. These inferred pressure ranges are consistent with measured H$_2$O–CO$_2$ saturation pressures of 160–290 MPa in plagioclase-hosted melt inclusions (Klug et al., 2020). Neither scenario, however, can explain the crystallization of quartz. MELTS simulations of adiabatic, fractional crystallization conditions suggest that ascent of rhyolite magma from >220 MPa at <790°C is required to crystallize quartz at <155 MPa (Figs. 10,12 and Table 9), consistent with the low entrapment pressures (90–160 MPa) of quartz-hosted melt inclusions interpreted to reflect late and shallow crystallization in a long-lived crystal mush (Klug et al., 2020).

The staged history of magma crystallization in compositionally diverse magma reservoirs suggested by our MELTS simulations
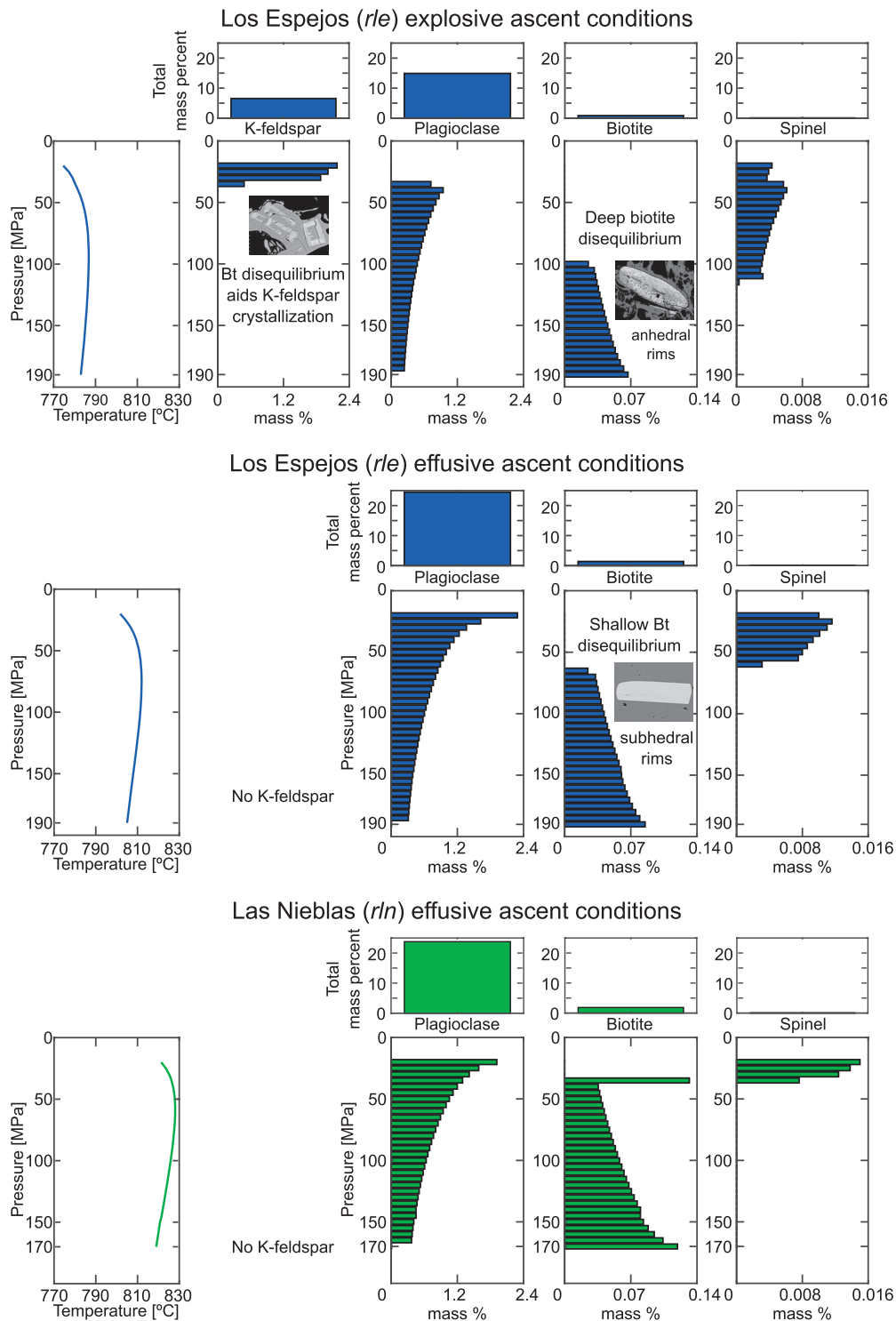
Fig. 13. Numerical simulations by MELTS of the ascent conditions of the *rle* explosive and effusive phases and the *rln* effusive phase. The suggested P–T paths consider information from adiabatic fractional crystallization and groundmass mineralogy. Biotite disequilibrium depth depends on the eruption style and is closely related to the crystallization of spinel, K-feldspar and to the biotite phenocryst shapes.

helps to explain the range of silica (64.6–72.6 wt.% SiO₂) and water (3.5–7.6 wt.%) contents measured in the *rdm* plagioclase-hosted melt inclusions (Klug *et al.*, 2020). The low but increasing fraction of mafic juvenile clasts and An-rich plagioclase through the *rdm* eruption sequence, the uniform major and trace element composition of the pumice clasts and the lack of complex zoning and disequilibrium textures in *rdm* phenocrysts (Fig. 4) further

suggests interaction of rhyolite magma with relatively small volumes of mafic-to-intermediate magmas shortly prior to or during the *rdm* eruption (Andersen *et al.*, 2017, 2018; Contreras-Hidalgo, 2020). Syn-eruptive tapping of previously isolated melt lenses has been suggested for other caldera-forming eruptions (e.g. Cashman & Giordano, 2014; Swallow *et al.*, 2018). In this scenario, the *rdm* eruption may have been triggered by protracted magma recharge

Table 10: Summary of the magma storage and ascent conditions forming the *rdm*, *rle* and *rln* rhyolite eruptions

	Rhyolite of LdM (*rdm*)	Rhyolite of Los Espejos (*rle*)	Rhyolite of Las Nieblas (*rln*)
Mineral assemblage	An_{20-59} plagioclase, hornblende & quartz	An_{22-23} plagioclase and biotite	An_{23-30} plagioclase and biotite
Composition(s) of magma reservoir(s)	High-silica andesite Dacite Rhyodacite	Rhyodacite	Rhyodacite
Composition(s) of interstitial melt(s)	Dacitic Rhyodacitic Rhyolitic	Rhyolitic	Rhyolitic
P–T storage conditions [MPa/°C]	Dacitic melt 300–350 / 890–945 Rhyodacitic melt 240–300 / 861–897 Rhyolitic melt 240–300 / 748–853 or 160–220 / 827–876	190–230 / 773–805	170–200 / 793–857
Variations in mineral phases or melt composition during ascent	Crystallization of quartz Increase of the silica content in melt	Colder magmas form K-feldspar and a deeper biotite disequilibrium	Pumice clasts (explosive) lack microcrysts.
More likely eruption trigger	Rhyolitic magma recharge in a shallow rhyolite chamber	Heating by wet mafic magma injection below the rhyodacitic mush	Pulsatory accumulation of fluids within a water-saturated reservoir
Syn-eruptive magma processes	Downward extraction of deeper, hotter intermediate-to-mafic magmas	>30 °C hotter magma eases the explosive-effusive eruption transition	Decreasing magma ascent rate leading the explosive-effusive transition.

at the <160 MPa rhyolite-melt reservoir(s) from >220 MPa melt-rich bodies of intermediate-to-mafic compositions, as suggested for other silicic explosive eruptions (e.g.Degruyter & Huber, 2014; Tramontano *et al.*, 2017). Subsequent syn-eruptive downward extraction of deeper, hotter intermediate-to-mafic magmas from connected magma reservoirs may explain the collapse of the crystal mush framework and subsequent caldera formation (Tarasewicz *et al.*, 2012; Cashman & Giordano, 2014). This scenario is also consistent with the common occurrence of glomerocrysts in the *rdm* pumice clasts (Fig. 4b,d) and the evacuation of granite clasts in the *rdm* ignimbrite deposit. Our MELTS modeling can simulate the mineral assemblage of the granite (An_{25-35} plagioclase and quartz) at 150 to 250 MPa, >55% crystals and near-eutectic (705–815°C) conditions (Fig. 10a).

Although zircon geochronology suggests that the shallow crystal-rich mush reservoir has produced rhyolite magma for the last 34–160 ky (Andersen *et al.*, 2019), the large ignimbrite and caldera-forming eruption of LdM (*rdm*) was the last to erupt both high-silica rhyolite and mafic-to-intermediate magmas; it also marks a transition to a new pattern of more frequent, smaller and less silicic rhyolite eruptions (Hildreth *et al.*, 2010; Hildreth, 2021). This shift suggests that the *rdm* eruption substantially perturbed the magmatic system, such that subsequent rhyolite differentiation and storage occurred at shallower depths without further mixing between rhyolite and mafic-to-intermediate magmas (e.g. Annen, 2009; Jackson *et al.*, 2018). In the next section, we analyze the role of storage conditions on the postignimbrite eruptions.

Storage and eruption conditions of the subplinian-effusive *rle* and *rln* rhyolites

The *rle* and *rln* rhyolite eruptions formed small (<3 km³ DRE; Fierstein, 2018; Gho *et al.*, 2019) pyroclastic fall and flow deposits and subsequent obsidian lava flows (∼1 km³ DRE; Cáceres *et al.*, 2018). Differing whole-rock, plagioclase, and zircon major and trace

element compositions between *rle* and *rln* suggest they formed at different storage conditions within the same mush system. For each *rle* and *rln* separately, common whole-rock and mineral compositions between juvenile pyroclasts and lavas suggests that magmas feeding both explosive and effusive phases come from the same melt-rich body (Fig. 3,4,6; Tables 1,2,3; Hildreth *et al.*, 2010;Andersen *et al.*, 2017; Cáceres *et al.*, 2018). The plagioclase-glass hygrometry and our MELTS simulations show that the limited range in plagioclase composition can be explained by crystallization over a limited range of pressure (170–230 MPa) and temperature (770–860°C), consistent with previous estimates from melt inclusions (Klug *et al.*, 2020) and two-oxide thermometry (Andersen *et al.*, 2017; Cáceres *et al.*, 2018). Our MELTS models further show that *rle* and *rln* magmas formed by modest crystallization (17–40%) of a dacitic to rhyodacitic (67.3–69.5 wt.% SiO_2) parental magma (Table 7). Crystal connectivity within the *rle* rhyolite batch is suggested by the presence of glomerocrysts with common An_{21-22} rims (Fig. 4). Similarities of water saturation pressures calculated using plagioclase outer rim compositions with those using plagioclase-hosted melt inclusions suggest that the plagioclase phenocrysts grew wholly in the same rhyodacitic magma reservoir. The lack of quartz is explained by storage temperatures ≥40°C hotter than the quartz saturation temperature (Fig. 11). Overall, the relatively high crystallization temperatures of the post-ignimbrite rhyolite magmas suggest that the LdM crystal mush is unlike the near-eutectic mushes characteristic of large high-silica rhyolite volcanic systems (Hildreth, 2021).

Both the *rle* and *rln* rhyolite magmas were saturated with volatiles and biotite (Figs. 8,11 and Table 7) and able to produce explosive eruptions. One possible eruption trigger is magma recharge accompanied by volatile exsolution (Degruyter & Huber, 2014; Tramontano *et al.*, 2017). In general, LdM rhyolites have become hotter and less silicic with time (Hildreth *et al.*, 2010; Andersen *et al.*, 2017, 2018), possibly a record of protracted heating by wet mafic magma injection below the rhyodacitic mush (e.g.

Andersen *et al.*, 2018; Cáceres *et al.*, 2018). Evidence for heating in the *rle* magma includes lower silica contents in groundmass glasses than in melt inclusions glasses (Fig. 3), anhedral biotite phenocrysts (Fig. 4) and Sr and Ba spikes in unzoned plagioclase crystals (Fig. 6) that suggest biotite breakdown (Barbey, 2007; Andersen *et al.*, 2018). These features, together with the relatively high CO_2 contents measured in melt inclusions (<370 ppm, the highest CO_2 contents observed in post-ignimbrite LdM rhyolites; Klug *et al.*, 2020), suggest that injection of a H_2O-rich and CO_2-rich mafic magma may have triggered the *rle* eruption. The higher temperature of the youngest rhyolite eruption, *rln*, together with the stepped-normal zoning of many plagioclase crystals (Fig. 6), further suggests pulsatory accumulation of melt and/or fluids supplied by deeper and hotter magmas followed by stages of cooling and stabilization (Huber *et al.*, 2011). We propose that these pulses were frequent enough to accumulate fluids and increase the pressure within the water-saturated rhyolite reservoirs, working as an external trigger of the *rln* subplinian eruption.

Rhyolite explosive-effusive transitions

Explosive-effusive transitions in silicic eruptions are governed by the magma ascent rate and the efficiency of outgassing during eruption and could reflect subtle differences in the magma storage conditions (Di Genova *et al.*, 2017; Cassidy *et al.*, 2018). Although analysis of the eruption dynamics is beyond the scope of this work, the groundmass textures and mineralogy of juvenile clasts (from the explosive phases) and lavas (from the effusive phases) provide insights into the role of the ascent conditions on the eruption transitions (e.g. Brugger & Hammer, 2010; Preece *et al.*, 2013, 2016; Riker *et al.*, 2015). For example, the absence of microcrysts in pumice from the *rdm* eruption (Fig. 5) indicates that magma ascent was sufficiently fast to avoid crystallization. The *rln* pumice also lacks phenocryst outer rims and microcrysts, in contrast to the ~25% crystals in the groundmass of the *rln* lavas (Figs. 4,5); this change in crystallinity suggests that the *rln* explosive-effusive transition was governed by a sharp decrease in magma ascent rate (Brugger & Hammer, 2010). In contrast, *rle* pumice clasts and lavas have similar groundmass crystallinity and mineralogy (Figs. 4,5). However, the euhedral biotite, lack of K-feldspar microcrysts and slightly higher crystallinity of the obsidian lavas suggests that the magma feeding the effusive phase was ~30°C hotter (Fig. 12). We propose that this temperature increase was produced by wet mafic recharge magma reheating the base of the rhyodacitic mush (e.g. Huber *et al.*, 2011; Brahm *et al.*, 2018). Explosive-effusive transitions caused by a temperature increase have also been suggested for Quizapu volcano, where the Plinian phase magma was 130°C cooler than the magma that fed preceding effusive activity (Ruprecht & Bachmann, 2010).

FINAL REMARKS AND EVALUATION OF THE CURRENT UNREST

Taken together, the large magnitude of the *rdm* eruption, the interpretation of a syn-eruptive downward extraction of more mafic magmas, and the predominance of rhyolites after *rdm* suggest both a substantial perturbation of the magmatic system and rapid reactivation of rhyolite generation. If the crystal mush conditions during the *rdm* eruption were like those currently observed geophysically (~450 km³, ~23 km³ of melt), the volume of the *rdm* rhyolite deposits (>17 km³ DRE) would reflect an almost complete extraction of the interstitial rhyolite melt from this region. Given that large silicic eruptions typically extract <30% of the reservoir

volume (White *et al.*, 2006; Miller *et al.*, 2017), a future *rdm*-sized eruption would require a much larger (>70 km³) reservoir of rhyolite melt.

The storage conditions of magmas that fed the *rle* and *rln* eruptions, in contrast, are similar to the small (<30 km³), mush-hosted magma batches currently imaged by geophysics (Miller *et al.*, 2017; Cordell *et al.*, 2020; Trevino *et al.*, 2021). Assuming that the rhyolite batches are compositionally in equilibrium with the surrounding crystal mush (Annen, 2009; Hildreth, 2021), our MELTS simulations indicate that the bulk composition of the crystal mush is dacitic to rhyodacitic (67.3–69.5 wt.% SiO_2) and that the storage pressure and crystallinity of both *rle* and *rln* magmas (170–230 MPa and 17–40% crystals) are consistent with those estimated for the current (C3) magma batches (100–250 MPa and 15–50% crystals; Miller *et al.*, 2017; Cordell *et al.*, 2018). Gravity analyses combined with MELTS simulations further indicate that the current inflation source is volatile saturated (Miller *et al.*, 2017; Andersen *et al.*, 2018), consistent with our estimates for the *rle* and *rln* magmas. If the conditions that fed the *rle* and *rln* eruptions were like those constrained by current geophysics, the volume of the *rle* and *rln* deposits (<4 km³ DRE) would require drainage of 10 to 17 vol.% of the magma reservoir, similar to calculations for post-caldera-forming eruptions from Yellowstone and Long Valley (White *et al.*, 2006; Miller *et al.*, 2017).

Direct injection of volatile-rich magmas and/or fluids from depth into shallow-stored rhyolite and/or the surrounding crystal mush is further suggested by a zone of anomalously high flux of distributed CO_2 at the surface (Sernageomin, REAV, 2021) together with volcanotectonic earthquakes at 1.6 to 8.4 km-depth and southwest of the inflation center (Cardona *et al.*, 2018). It is possible that such injections triggered the *rle* and *rln* eruptions. The similarity of the estimated volume, water-saturated conditions and crystallinity (~30 km³, 5–6 wt% H_2O, 30–50% crystals; Miller *et al.*, 2017) of the geophysically inferred reservoir today with the petrologically determined storage conditions of the *rle* and *rln* magmas suggest that if fluids and melts arriving from depth were to trigger an eruption in the near future, this would most likely form a subplinian to moderate Plinian column and lava flow(s). From this, we suggest that continued geophysical and geochemical monitoring of the LdM magmatic system is important for identifying key eruption precursors. Furthermore, our conclusion that the next eruption of LdM is likely to be of a similar size and style as other post-*rdm* eruptions provides likely eruption scenarios for hazard mitigation planning.

SUPPLEMENTARY DATA

Supplementary Data are available at *Journal of Petrology* online.

DATA AVAILABILITY STATEMENT

The data underlying this article are available in the article and in its online supplementary material.

References

Andersen, N. L., Singer, B. S., Jicha, B. R., Beard, B. L., Johnson, C. M. & Licciardi, J. M. (2017). Pleistocene to Holocene growth of a large upper crustal rhyolitic magma reservoir beneath the active Laguna del Maule volcanic field, Central Chile. *Journal of Petrology* **58**, 85–114. https://doi.org/10.1093/petrology/egx006.

Andersen, N. L., Singer, B. S., Costa, F., Fournelle, J., Herrin, J. S. & Fabbro, G. N. (2018). Petrochronologic perspective on rhyolite volcano unrest at Laguna del Maule, Chile. *Earth and Planetary Science Letters* **493**, 57–70. https://doi.org/10.1016/j.epsl.2018.03.043.

Andersen, N. L., Singer, B. S. & Coble, M. A. (2019). Repeated rhyolite eruption from heterogeneous hot zones embedded within a cool, shallow magma reservoir. *Journal of Geophysical Research* **124**, 2582–2600. https://doi.org/10.1029/2018JB016418.

Annen, C. (2009). From plutons to magma chambers: thermal constraints on the accumulation of eruptible silicic magma in the upper crust. *Earth and Planetary Science Letters* **284**, 409–416. https://doi.org/10.1016/j.epsl.2009.05.006.

Bachmann, O. & Bergantz, G. W. (2004). On the origin of crystal-poor rhyolites: extracted from batholithic crystal mushes. *Journal of Petrology* **45**(8), 1565–1582. https://doi.org/10.1093/petrology/egh019.

Bai, T., Thurber, C., Lanza, F., Singer, B. S., Bennington, N., Keranen, K. & Cardona, C. (2020). Teleseismic tomography of the Laguna del Maule volcanic field in Chile. *Journal of Geophysical Research: Solid Earth* **125**(8), e2020JB019449.

Barbey, P. (2007). Diffusion-controlled biotite breakdown reaction textures at the solid/liquid transition in the continental crust. *Contributions to Mineralogy and Petrology* **154**(6), 707–716. https://doi.org/10.1007/s00410-007-0220-x.

Barboni, M., Boehnke, P., Schmitt, A. K., Harrison, T. M., Shane, P., Bouvier, A.-S. & Baumgartner, L. (2016). Warm storage for arc magmas. *Proceedings of the National Academy of Sciences* **113**(49), 13959–13964. https://doi.org/10.1073/pnas.1616129113.

Barker, S. J., Wilson, C. J. N., Morgan, D. J. & Rowland, J. V. (2016). Rapid priming, accumulation, and recharge of magma driving recent eruptions at a hyperactive caldera volcano. *Geology* **44**, 323–326. https://doi.org/10.1130/G37382.1.

Bégué, F., Gualda, G. A., Ghiorso, M. S., Pamukcu, A. S., Kennedy, B. M., Gravley, D. M., Deering, C. D. & Chambefort, I. (2014). Phase-equilibrium geobarometers for silicic rocks based on rhyolite-MELTS. Part 2: application to Taupo volcanic zone rhyolites. *Contributions to Mineralogy and Petrology* **168**(5), 1082. https://doi.org/10.1007/s00410-014-1082-7.

Biggs, J. & Pritchard, M. E. (2017). Global volcano monitoring: what does it mean when volcanoes deform? *Elements* **13**(1), 17–22. https://doi.org/10.2113/gselements.13.1.17.

Bindeman, I. N. & Simakin, A. G. (2014). Rhyolites—hard to produce, but easy to recycle and sequester: integrating microgeochemical observations and numerical models. *Geosphere* **10**(5), 930–957. https://doi.org/10.1130/GES00969.1.

Brahm, R., Parada, M. A., Morgado, E., Contreras, C. & McGee, L. E. (2018). Origin of Holocene trachyte lavas of the Quetrupillán volcanic complex, Chile: examples of residual melts in a rejuvenated crystalline mush reservoir. *Journal of Volcanology and Geothermal Research* **357**, 163–176. https://doi.org/10.1016/j.jvolgeores.2018.04.020.

Brugger, C. R. & Hammer, J. E. (2010). Crystal size distribution analysis of plagioclase in experimentally decompressed hydrous rhyodacite magma. *Earth and Planetary Science Letters* **300**(3–4), 246–254. https://doi.org/10.1016/j.epsl.2010.09.046.

Cáceres, F., Castruccio, Á. & Parada, M. A. (2018). Morphology, effusion rates, and petrology of postglacial lavas of Laguna del Maule volcanic field, Chilean Andes, and implications for their plumbing system. *Geochemistry, Geophysics, Geosystems* **19**(12), 4925–4944. https://doi.org/10.1029/2018GC007817.

Cardona, C., Tassara, A., Gil-Cruz, F., Lara, L., Morales, S., Kohler, P. & Franco, L. (2018). Crustal seismicity associated to rapid surface uplift at Laguna del Maule volcanic complex, southern volcanic zone of the Andes. *Journal of Volcanology and Geothermal Research* **353**, 83–94. https://doi.org/10.1016/j.jvolgeores.2018.01.009.

Cashman, K. V. & Giordano, G. (2014). Calderas and magma reservoirs. *Journal of Volcanology and Geothermal Research* **288**, 28–45. https://doi.org/10.1016/j.jvolgeores.2014.09.007.

Cashman, K. V., Sparks, R. S. J. & Blundy, J. D. (2017). Vertically extensive and unstable magmatic systems: a unified view of igneous processes. *Science* **355**(6331), eaag3055. https://doi.org/10.1126/science.aag3055.

Cassidy, M., Manga, M., Cashman, K. & Bachmann, O. (2018). Controls on explosive-effusive volcanic eruption styles. *Nature Communications* **9**(1), 2839. https://doi.org/10.1038/s41467-018-05293-3.

Castro, J. M. & Dingwell, D. B. (2009). Rapid ascent of rhyolitic magma at Chaitén volcano, Chile. *Nature* **461**(7265), 780–783. https://doi.org/10.1038/nature08458.

Cembrano, J. & Lara, L. (2009). The link between volcanism and tectonics in the southern volcanic zone of the Chilean Andes: a review. *Tectonophysics* **471**(1–2), 96–113. https://doi.org/10.1016/j.tecto.2009.02.038.

Contreras-Hidalgo, C. (2020) *Silicic Eruptive Transitions of Laguna del Maule* PhD Thesis. UK: University of Bristol.

Cordell, D., Unsworth, M. J. & Díaz, D. (2018). Imaging the Laguna del Maule volcanic field, Central Chile using magnetotellurics: evidence for crustal melt regions laterally-offset from surface vents and lava flows. *Earth and Planetary Science Letters* **488**, 168–180. https://doi.org/10.1016/j.epsl.2018.01.007.

Cordell, D., Unsworth, M. J., Lee, B., Díaz, D., Bennington, N. L. & Thurber, C. H. (2020). Integrating magnetotelluric and seismic images of silicic magma systems: a case study from the Laguna del Maule volcanic field, Central Chile. *Journal of Geophysical Research: Solid Earth* **125**(11), e2020JB020459.

Deer, W A, Howie, R A, Zussman, J (2013). *An introduction to the rock-forming minerals*. Longman Group UK.

Degruyter, W. & Huber, C. (2014). A model for eruption frequency of upper silicic magma chambers. *Earth and Planetary Science Letters* **403**, 117–130. https://doi.org/10.1016/j.epsl.2014.06.047.

Di Genova, D., Kolzenburg, S., Wiesmaier, S., Dallanave, E., Neuville, D. R., Hess, K. U. & Dingwell, D. B. (2017). A compositional tipping point governing the mobilization and eruption style of rhyolitic magma. *Nature* **552**(7684), 235–238. https://doi.org/10.1038/nature24488.

Druitt, T. H., Costa, F., Deloule, E., Dungan, M. & Scaillet, B. (2012). Decadal to monthly timescales of magma transfer and reservoir growth at a caldera volcano. *Nature* **482**(7383), 77–80. https://doi.org/10.1038/nature10706.

Erdmann, S., Martel, C., Pichavant, M. & Kushnir, A. (2014). Amphibole as an archivist of magmatic crystallization conditions: problems, potential, and implications for inferring magma storage prior to the paroxysmal 2010 eruption of mount Merapi, Indonesia. *Contributions to Mineralogy and Petrology* **167**(6), 1016. https://doi.org/10.1007/s00410-014-1016-4.

Feigl, K. L., Le Mével, H., Tabrez Ali, S., Córdova, L., Andersen, N. L., DeMets, C. & Singer, B. S. (2014). Rapid uplift in Laguna del Maule volcanic field of the Andean southern volcanic zone (Chile) 2007–2012. *Geophysical Journal International* **196**(2), 885–901. https://doi.org/10.1093/gji/ggt438.

Fierstein, J. (2018) *Postglacial eruptive history established by mapping and tephra stratigraphy provides perspectives on magmatic system beneath Laguna del Maule, Chile, Presented at: AGU Chapman Conference on Merging Geophysical, Petrochronologic, and Modeling Perspectives of Large Silicic Magma Systems*. Chile: Quinamavida.

Garibaldi, N., Tikoff, B., Peterson, D., Davis, J. R. & Keranen, K. (2020). Statistical separation of tectonic and inflation-driven components of deformation on silicic reservoirs, Laguna del Maule volcanic field, Chile. *Journal of Volcanology and Geothermal Research* **389**, 106744. https://doi.org/10.1016/j.jvolgeores.2019.106744.

Gelman, S. E., Gutiérrez, F. J & Bachmann, O. (2013). On the longevity of large upper crustal silicic magma reservoirs. *Geology* **41**(7), 759–762. https://doi.org/10.1130/G34241.1.

Ghiorso, M. S. & Gualda, G. A. (2015). An H2O–CO2 mixed fluid saturation model compatible with rhyolite-MELTS. *Contributions to Mineralogy and Petrology* **169**(6), 53. https://doi.org/10.1007/s00410-015-1141-8.

Gho, R., Sruoga, P., Amigo, Á., Fierstein, J., Elissondo, M., Kaufman, J., Toloza, V. & Calderón, R. (2019). Peligros del Complejo Volcánico Laguna del Maule, región del Maule, Chile – Provincias de Mendoza y Neuquén, Argentina. *Servicio Nacional de Geología y Minería – Servicio Geológico Minero Argentino, Publicación Geológica Multinacional* , 1 mapa escala 1:75.000.

Gualda, G. A., Ghiorso, M. S., Lemons, R. V. & Carley, T. L. (2012). Rhyolite-MELTS: a modified calibration of MELTS optimized for silica-rich, fluid-bearing magmatic systems. *Journal of Petrology* **53**(5), 875–890. https://doi.org/10.1093/petrology/egr080.

Hildreth, W. (2021). Comparative rhyolite systems: inferences from vent patterns and eruptive Episodicities: eastern California and Laguna del Maule. *Journal of Geophysical Research: Solid Earth* , e2020JB020879.

Hildreth, W., Godoy, E., Fierstein, J. & Singer, B. S. (2010) *Laguna del Maule volcanic field: eruptive history of a Quaternary basalt to rhyolite distributed volcanic field on the Andean range crest in central Chile.* Boletin: Servicio Nacional de Geología y Minería, p.63.

Holland, T. & Blundy, J. (1994). Non-ideal interactions in calcic amphiboles and their bearing on amphibole-plagioclase thermometry. *Contributions to Mineralogy and Petrology* **116**(4), 433–447. https://doi.org/10.1007/BF00310910.

Huber, C., Bachmann, O. & Dufek, J. (2011). Thermo-mechanical reactivation of locked crystal mushes: melting-induced internal fracturing and assimilation processes in magmas. *Earth and Planetary Science Letters* **304**, 443–454. https://doi.org/10.1016/j.epsl.2011.02.022.

Jackson, M. D., Blundy, J. & Sparks, R. S. J. (2018). Chemical differentiation, cold storage and remobilization of magma in the Earth's crust. *Nature* **564**(7736), 405–409. https://doi.org/10.1038/s41586-018-0746-2.

Klug, J. D., Singer, B. S., Kita, N. T. & Spicuzza, M. J. (2020). Storage and evolution of Laguna del Maule rhyolites: insight from volatile and trace element contents in melt inclusions. *Journal of Geophysical Research: Solid Earth* **125**(8), e2020JB019475.

Le Bas, M., Maitre, R. L., Streckeisen, A., Zanettin, B., Subcommission, I. U. G. S. & on the Systematics of Igneous Rocks (1986). A chemical classification of volcanic rocks based on the total alkali-silica diagram. *Journal of Petrology* **27**(3), 745–750. https://doi.org/10.1093/petrology/27.3.745.

Le Mével, H., Córdova, L., Cardona, C. & Feigl, K. L. (2021). Unrest at the Laguna del Maule volcanic field 2005–2020: renewed acceleration of deformation. *Bulletin of Volcanology* **83**(6), 1–9. https://doi.org/10.1007/s00445-021-01457-0.

López-Escobar, L., Cembrano, J. & Moreno, H. (1995). Geochemistry and tectonics of the Chilean southern Andes basaltic quaternary volcanism (37-46 S). *Andean Geology* **22**(2), 219–234.

Matjuschkin, V., Brooker, R. A., Tattitch, B., Blundy, J. D. & Stamper, C. C. (2015). Control and monitoring of oxygen fugacity in piston cylinder experiments. *Contributions to Mineralogy and Petrology* **169**(1), 9. https://doi.org/10.1007/s00410-015-1105-z.

Miller, C. A., Williams-Jones, G., Fournier, D. & Witter, J. (2017). 3D gravity inversion and thermodynamic modelling reveal properties of shallow silicic magma reservoir beneath Laguna del Maule, Chile. *Earth and Planetary Science Letters* **459**, 14–27. https://doi.org/10.1016/j.epsl.2016.11.007.

Peccerillo, A. & Taylor, S. R. (1976). Geochemistry of Eocene calc-alkaline volcanic rocks from the Kastamonu area, northern Turkey. *Contributions to Mineralogy and Petrology* **58**(1), 63–81. https://doi.org/10.1007/BF00384745.

Preece, K., Barclay, J., Gertisser, R. & Herd, R. A. (2013). Textural and micro-petrological variations in the eruptive products of the 2006 dome-forming eruption of Merapi volcano, Indonesia: implications for sub-surface processes. *Journal of Volcanology and Geothermal Research* **261**, 98–120. https://doi.org/10.1016/j.jvolgeores.2013.02.006.

Preece, K., Gertisser, R., Barclay, J., Charbonnier, S. J., Komorowski, J. C. & Herd, R. A. (2016). Transitions between explosive and effusive phases during the cataclysmic 2010 eruption of Merapi volcano, Java, Indonesia. *Bulletin of Volcanology* **78**(8), 54–16. https://doi.org/10.1007/s00445-016-1046-z.

Putirka, K. (2016). Amphibole thermometers and barometers for igneous systems, and some implications for eruption mechanisms of felsic magmas at arc vol-canoes. *American Mineralogist* **101**, 841–858. https://doi.org/10.2138/am-2016-5506.

Ridolfi, F., Renzulli, A. & Puerini, M. (2010). Stability and chemical equilibrium of amphibole in calc-alkaline magmas: an overview, new thermobarometric formulations and application to subduction-related volcanoes. *Contributions to Mineralogy and Petrology* **160**(1), 45–66. https://doi.org/10.1007/s00410-009-0465-7.

Riker, J. M., Blundy, J. D., Rust, A. C., Botcharnikov, R. E. & Humphreys, M. (2015). Experimental phase equilibria of a Mount St. Helens rhyodacite: a framework for interpreting crystallization paths in degassing silicic magmas. *Contributions to Mineralogy and Petrology* **170**(1), 1–22.

Rojas, A., Sruoga, P., Lamberti, M. C., Agusto, M., Tondreau, J., Mendoza, N., Daniele, L. & Morata, D. (2022). Unravelling the hydrothermal system of Laguna del Maule restless volcanic field, in the Andean southern volcanic zone (36° 10′ S). *Journal of Volcanology and Geothermal Research* **424**, 107498. https://doi.org/10.1016/j.jvolgeores.2022.107498.

Rubin, A. E., Cooper, K. M., Till, C. B., Kent, A. J. R., Costa, F., Bose, M., Gravley, D., Deering, C. & Cole, J. (2017). Rapid cooling and cold storage in a silicic magma reservoir recorded in individual crystals. *Science* **356**, 1154–1156. https://doi.org/10.1126/science.aam8720.

Ruprecht, P. & Bachmann, O. (2010). Pre-eruptive reheating during magma mixing at Quizapu volcano and the implications for the explosiveness of silicic arc volcanoes. *Geology* **38**(10), 919–922. https://doi.org/10.1130/G31110.1.

Schipper, C. I., Castro, J. M., Tuffen, H., James, M. R. & How, P. (2013). Shallow vent architecture during hybrid explosive–effusive activity at Cordón Caulle (Chile, 2011–12): evidence from direct observations and pyroclast textures. *Journal of Volcanology and Geothermal Research* **262**, 25–37. https://doi.org/10.1016/j.jvolgeores.2013.06.005.

Self, S. (2006). The effects and consequences of very large explosive volcanic eruptions. *Philosophical Transactions of the Royal Society A: Mathematical, Physical and Engineering Sciences* **364**(1845), 2073–2097. https://doi.org/10.1098/rsta.2006.1814.

Self, S. & Blake, S. (2008). Consequences of explosive supereruptions. *Elements* **4**(1), 41–46. https://doi.org/10.2113/GSELEMENTS.4.1.41.

SERNAGEOMIN (2020). Reporte especial de Actividad Volcánica (REAV). *Región del Maule* , 18 de Junio de 2020. http://sitiohistorico.sernageomin.cl/volcan.php?iId=53 (accessed 7 January 2022).

SERNAGEOMIN (2021). Reporte especial de Actividad Volcánica (REAV). *Región del Maule* , 14 de Mayo de 2021. http://sitiohistorico.sernageomin.cl/volcan.php?iId=53 (accessed 7 January 2022).

Swallow, E. J., Wilson, C. J., Myers, M. L., Wallace, P. J., Collins, K. S. & Smith, E. G. (2018). Evacuation of multiple magma bodies and the onset of caldera collapse in a supereruption, captured in glass and mineral compositions. *Contributions to Mineralogy and Petrology* **173**(4), 1–22. https://doi.org/10.1007/s00410-018-1459-0.

Tarasewicz, J., Brandsdóttir, B., White, R. S., Hensch, M. & Thorbjarnardóttir, B. (2012). Using microearthquakes to track repeated magma intrusions beneath the Eyjafjallajökull stratovolcano, Iceland. *Journal of Geophysical Research: Solid Earth* **117**(B9). https://doi.org/10.1029/2011JB008751.

Till, C. B., Vazquez, J. A. & Boyce, J. W. (2015). Months between rejuvenation and volcanic eruption at Yellowstone caldera, Wyoming. *Geology* **43**(8), 695–698. https://doi.org/10.1130/G36862.1.

Tramontano, S., Gualda, G. A. & Ghiorso, M. S. (2017). Internal triggering of volcanic eruptions: tracking overpressure regimes for giant magma bodies. *Earth and Planetary Science Letters* **472**, 142–151. https://doi.org/10.1016/j.epsl.2017.05.014.

Trevino, S. F., Miller, C. A., Tikoff, B., Fournier, D. & Singer, B. S. (2021). Multiple, coeval silicic magma storage domains beneath the Laguna Del Maule volcanic field inferred from gravity investigations. *Journal of Geophysical Research: Solid Earth* **126**(4), e2020JB020850.

Wark, D. A., Hildreth, W., Spear, F. S., Cherniak, D. J. & Watson, E. B. (2007). Pre-eruption recharge of the bishop magma system. *Geology* **35**(3), 235–238. https://doi.org/10.1130/G23316A.1.

Waters, L. E. & Lange, R. A. (2015). An updated calibration of the plagioclase-liquid hygrometer-thermometer applicable to basalts through rhyolites. *American Mineralogist* **100**(10), 2172–2184. https://doi.org/10.2138/am-2015-5232.

Wespestad, C., Thurber, C. H., Andersen, N. L., Singer, B. S., Cardona, C., Zeng, X., Bennington, N. L., Keranen, K., Peterson, D. E., Cordell, D., Unsworth, M., Miller, C & Williams-Jones, G. (2019). Magma body beneath Laguna del Maule volcanic field imaged with surface wave tomography. *Journal of Geophysical Research: Solid Earth* **124**. https://doi.org/10.1029/2018JB016485.

White, S. M., Crisp, J. A. & Spera, F. J. (2006). Long-term volumetric eruption rates and magma budgets. *Geochemistry, Geophysics, Geosystems* **7**(3). https://doi.org/10.1029/2005GC001002.

Wilson, C. J. N. (2017). Volcanoes: characteristics, tipping points, and those pesky unknown unknowns. *Elements* **13**(1), 41–46. https://doi.org/10.2113/gselements.13.1.41.

Wotzlaw, J.-F., Bindeman, I. N., Watts, K. E., Schmitt, A. K., Caricchi, L. & Schaltegger, U. (2014). Linking rapid magma reservoir assembly and eruption trigger mechanisms at evolved Yellowstone-type supervolcanoes. *Geology* **42**(9), 807–810. https://doi.org/10.1130/G35979.1.